POLITECNICO DI TORINO

Master of Science Degree in Renewable Energy Systems

Master of Science Thesis

CFD analysis of a CPC structure for LFC applications

Supervisors

Prof. Roberto ZANINO

Prof. Mattia CAGNOLI

PhD. Mehdi SHOKRNIA

Candidate

Giovanni SUSCA

A.y. 2024/25

Table of Contents

List of Tables

List of Figures

Abstract

In the context of Concentrated Solar Power (CSP), the Linear Fresnel Collector (LFC) system is a promising and reliable technology. In this document, a detailed study is conducted, with the aim to assess the performances of a LFC receiver unit, in several environmental scenarios, and in a wide range of temperature. The receiver unit typically encompasses an absorber tube and a Compound Parabolic Concentrator (CPC), designed to insulate the environment around the tube and to reconcentrate incident solar light, which is not able to reach directly the absorber. In this project the absorber tube is not present, its role is being simulated by the CPC cavity itself. Multiple CFD simulations are describing in detail the behavior of the system by means of a 2D model, that solves the energy balance between the receiver and the coolant (external air). The 2D model requires an accurate computational fluid dynamic (CFD) analysis, implemented on the commercial $STAR-CCM+software, withthegoaltodeterminetheusefulheattransferredtotheexternalair, andtheconv$ $500řC), providingdifferentsightsonthepossibleworkingfluidswhichareallowedtobeused; moltensa$ + 40%wt. KNO_3), working in the temperature range 290-500 °C , and two diathermic oils (Therminol VP-1 and DelcoTerm Solar E15), respectively working in the temperature range 290-400 ℃ and 200-300 ℃. The heat losses evaluation, following the radial direction, gives an outlook of the performance of system, and puts attention on the radiative and convective relative share and weight. The final aim of the project is to understand if the design of the new introduced CPC is competitive with other previous, and to develop a new correlation suitable for the adopted geometry.

Introduction

The aim of this thesis is to focus on the advantages provided by the introduction of a Compound Parabolic Collector (CPC) in Linear Fresnel Collector (LFC) systems, in the context of the exploitation of the solar power, on large scale. The technical aspects are discussed, with the assessment through Computational Fluid Dynamics (CFD) models of a specific CPC design.

In this chapter, some background information is provided, to explain the potential of Concentrated Solar Power (CSP) technology in the future energy scenario.

Climate change

Nowadays, the focus on a topic, as the climate change, is fundamental for imagining a solid near present and a bright future. It is well known how the impacts of human emissions, in the last century and in the current one, have compromised global next social and economical scenarios.

Human-caused greenhouse gas (GHG) emissions drive climate change. About 60% of the GHG emissions come from just 10 countries, while the 100 least emitting countries contribute less than 3%. As shown in Figure 1, energy is the sector that participates the most to global emissions, almost for three quarters, 37.4 Gt CO_2e [1]. Specifically, only China and the United States together account for %40 of total emissions.

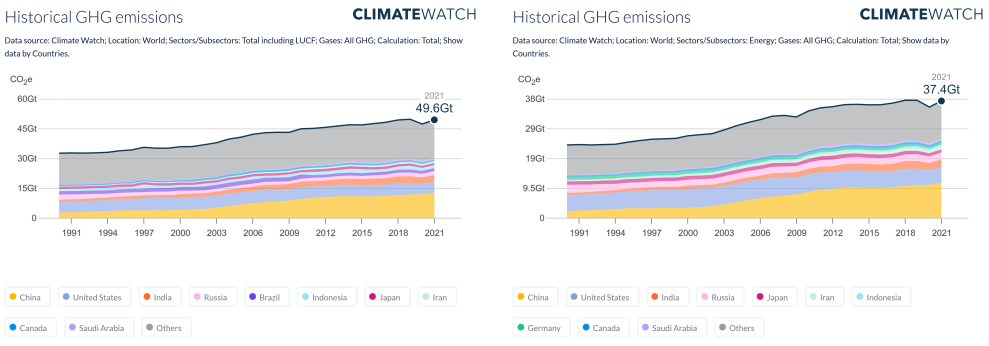

Figure 1: Historical GHG emission trend with energy contribution

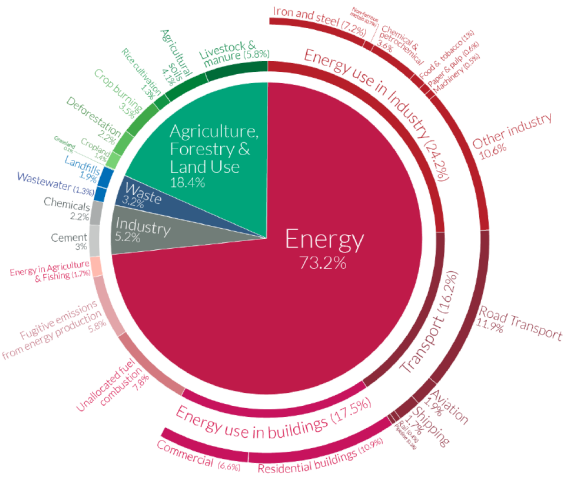

Figure 2: GHG emission by sector

The Figure 2 represents the share of each sector in the total GHG emission amount [2].
As said before, the energy sector is the most impactful, specifically, its use in industries, in buildings and in transports.

It is followed by agriculture, forestry and land use sectors, which have a double impact on the actual scenario because is the natural sink of CO_2e emissions.

Obviously, the rising trend of GHG emissions causes an increase in the global surface temperature, as shown in Figure 3.

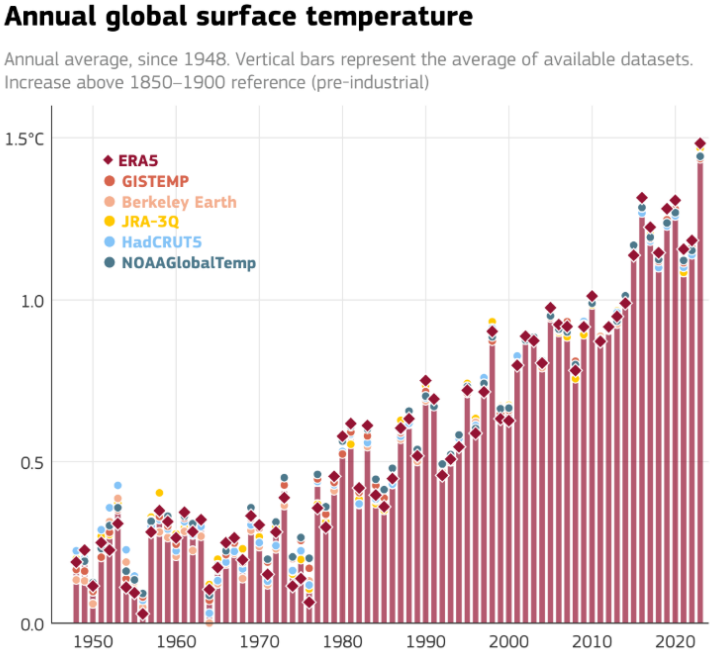

Figure 3: Global temperature trend with respect to preindustrial age

In 2024, Earth's surface was measured to be 1.47 °C warmer than in the late nineteenth century (1850-1900), namely preindustrial age.

The 10 most recent years have been registered as the warmest in history, specifically the last one got over the famous 2 °C bound several times, by now considering almost normal the exceeding of the 1.5 °C bound [3].

Decarbonization programs

The decarbonization of the energy sector has been a critical area of research for several years. This process, which involves reducing or eliminating carbon emissions from energy production and consumption, is considered essential in the climate change debate.

The first global efforts to manage and stabilize the concentration of GHGs in the atmosphere began in earnest at the Earth Summit held in Rio de Janeiro in 1992. This summit brought together a large number of nations with the goal of addressing various environmental challenges. One of the main outcomes of this summit was the adoption of the United Nations Framework Convention on Climate Change (UNFCCC), a treaty aimed at reducing global GHG emissions and promoting sustainable development. The agreement was significant because it marked the beginning of coordinated international efforts to combat climate change. Countries that signed the UNFCCC committed to taking measures to limit emissions and to work together in the pursuit of long-term climate stability.

The UNFCCC has been the foundation for subsequent climate agreements, most notably the Kyoto Protocol and the Paris Agreement.

Kyoto Protocol

The Kyoto Protocol is an international agreement aimed at tackling climate change. It was the first major global treaty, where more than 160 industrialized nations agreed to reduce the emissions of GHGs.

The protocol was adopted in Kyoto, Japan, in 1997, during the third Conference of Parties (COP 3), and became legally binding in 2005, after the ratification of Russia.

The Kyoto Protocol committed industrialized countries and countries with economies in transition to reduce their greenhouse gas emissions by 5.2% compared to 1990 levels by 2012.

However, the Kyoto Protocol did not impose emission reduction commitments on all signatory countries, but only on those listed in Annex I.

The Annex I group consists of 39 countries, including OCSE countries and some nations with transitioning economies. The decision was made because they were given a greater responsibility for reducing emissions, because they were historically the main contributors to climate change.

Furthermore, the responsibility among the Annex I countries was not distributed equally, but was assigned based on factors like, the level of industrial development, incomes, efficiency of the energy sector.

Specifically, the European Union (EU) was committed to reduce, by 8%, CO_2e emissions. This target was then split among each EU state. The target for Italy was set at 6.5%.

To ensure flexibility in the effective realization of the Protocol and to minimize the overall economic burden on the countries involved, the Protocol introduced three mechanisms:

- **Emissions Trading (ET)**: It allows countries that reduce their emissions

beyond their targets to sell their surplus emissions credits to countries that have not been able to meet their targets.

- **Joint Implementation (JI)**: It allows Annex I countries to work together in achieving their emission reduction targets by agreeing on a different distribution of obligations. They can transfer or purchase emission reduction units ($ERUs$) from each other through joint projects.
- **Clean Development Mechanism (CDM)**: It is based on the gain of Certified Emission Reductions (CERs), which are certifications that allows to cover a percentage of the target. Annex I countries, or private entities, can help to finance projects that aim to reduce emissions in less developed nations. In return they gain CERs. [4].

As seen, there were several ways to deceive each constraint. In some cases, the aim of reducing current emissions resulted in a net zero balance, due to the frequent implementation of market mechanisms by the most emitting counties.

Additionally, it is important to underline that the United States, which accounts for more than one third of global emissions, did not ratify the Protocol, certifying how the climate change was not a priority for most of the nations involved and not.

Paris Agreement

Paris Agreement is the following treaty on climate change, after Kyoto Protocol. It was adopted by 196 parties at COP 21, in Paris, in 2015, and formally started in 2016.

To reach the goals of Paris Agreement emissions must reach net-zero target in the second half of the century, limiting global warming below 2°C and trying to fix the increasing temperature trend to 1.5°C.

The Paris Agreement works on five-year cycles. Since 2020, countries have been submitting their national climate action plans, known as nationally determined contributions (NDCs), to reduce their emissions. Each successive NDC is meant to accomplish a higher degree of ambition compared to previous versions.

Countries are also "invited" to communicate “mid-century long-term low GHG emissions development strategies” (long-term strategies or LTS) [5].

Not all provisions inside the agreement are legally binding, in fact, each party has the freedom to set emission reduction targets, or to plan their economy without following determined constraints. The only legal obligation is the submission of a NDC report every five years [6].

Indeed, following the same behavior had with Kyoto Protocol, the United States withdrew from the Paris agreement in 2020, rejoined in 2021, and announced the withdrawal again in 2025, as evidence of a still soft behavior in the scope of climate change.

Forecasts are not encouraging, actions have to be taken as soon as possible to face the global warming. All countries have to put apart their economical interests in the energy sector, and work together to reach a more sustainable global scenario, for the planet and for the safety of each inhabitant of the globe.

Every day the world is witness of environmental cataclysms with devastating consequences, from small to large scale. Obviously, continuing to follow this trend, will favors the frequency of these extreme events, that must to be avoided.

To limit global warming to 1.5°C, greenhouse gases emission must decline around 43% by 2030, that concretely, seems to be impossible from today prospective. Thus, to meet a zero net balance by the end of the century, and for avoiding other future catastrophic scenarios, some specific routes have to be followed, as shown in Figure 4.

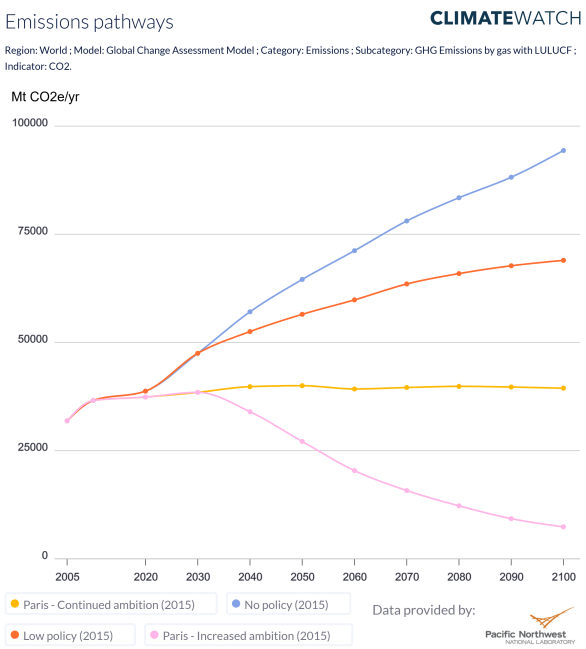

Figure 4: Emission scenarios

It is possible to notice how future scenarios with no policy or low policy are going to drive the Earth to an irreversible path.
The Earth's environment, including soils, forests, and oceans, absorbs a significant amount of carbon dioxide (CO2) every year. This process of absorption is known as carbon sequestration. Recent estimations suggest that the Earth's environment absorbs about 25 billion metric tons of $CO2_e$ per year, thus even a Paris-continued ambition scenario won't be enough.

Renewable energy sources

Transitioning away from fossil fuels to sustainable energy sources is one of the key challenges of the 21^{st} century. This challenge has emphasized the importance of renewable sources such as solar energy.

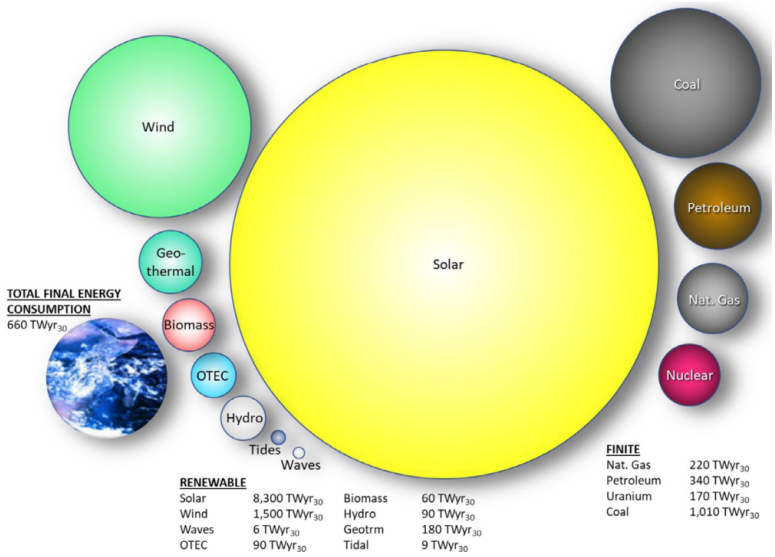

Figure 5: Renewable energy reserves and finite energy resources over the next 30 years in comparison to the estimated total demand

A look at the supply-side energy reserves for the planet, as shown in Figure 5, reveals that solar energy is by far the largest energy resource available on Earth, even after considering factors like reasonable deployment restrictions and current levels of achievable conversion efficiencies. To provide a rough estimate, solar energy has the potential to supply approximately twelve times the total primary energy demand of the world over a period of thirty years. In simpler terms, this means that solar energy could easily meet the global energy needs for the next three decades, and still provide much more than what is currently consumed [7].

The aggregate of the other renewable sources, not considering the solar energy, owns the potential to substitute the overall energy of the world fossil reservoir. Especially wind power is able to cover alone the total final energy consumption of the Earth for the next thirty years.

Since 2010, there has been a significant decrease in the costs of renewable power generation, despite the challenges imposed by rising materials and equipment costs. This is a remarkable achievement, highlighting the continued progress and economic competitiveness of renewable energy technologies, as highlighted by the International Renewable Energy Agency (IRENA) in Tab 1, [8].

	Total installed costs			Capacity factor			LCOE		
	2022 (USD/kW)			(%)			2022 (USD/kWh)		
	2010	2022	%	2010	2022	%	2010	2022	%
Bioenergy	2904	2162	-26%	72	72	1%	0.082	0.061	-25%
Geothermal	2904	3478	20%	87	85	-2%	0.053	0.056	6%
Hydropower	1407	2881	105%	44	46	4%	0.042	0.061	47%
Solar PV	5124	876	-83%	14	17	23%	0.445	0.049	-89%
CSP	10082	4274	-58%	30	36	19%	0.380	0.118	-69%
Onshore wind	2179	1274	-42%	27	37	35%	0.107	0.033	-69%
Offshore wind	5217	3461	-34%	38	42	10%	0.197	0.081	-59%

Table 1: Total installed cost, capacity factor and LCOE RES trends, 2010 and 2022

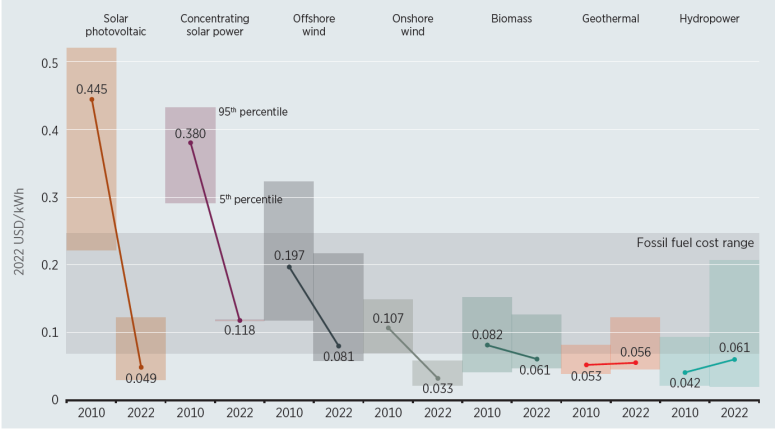

Figure 6: Renewable power generation LCOE versus fossil fuels

As of today, renewable power systems have already reached a point where their Levelised Cost of Electricity (LCOE) is lower than that of fossil fuels, making them more cost-efficient in comparison, as Figure 6 shows. This means, in terms of generation of electricity, that renewable energy sources are now less expensive than fossil fuel-based systems.

The cumulative impact of renewable energy, globally deployed since the year 2000, has saved globally an impressive EUR 500 billion in fuel costs within the electricity sector alone [8].

This significant trend highlights the growing importance of renewable energy in reducing the world's dependence on fossil fuels. The widespread adoption of renewable energy has wider economic implications. By shifting away from volatile fossil fuel markets, countries can mitigate the risk of price spikes and supply disruptions, ensuring a more stable and resilient economy.

As countries continue to make substantial investments in clean energy, they not only benefit from affordable and cost-competitive sources but also reduce their dependence on external exporting countries, thus enhancing national energy security. Renewable energy transition is driving economic growth, creating jobs, fostering innovation, and providing energy access to more people.

CSP technology

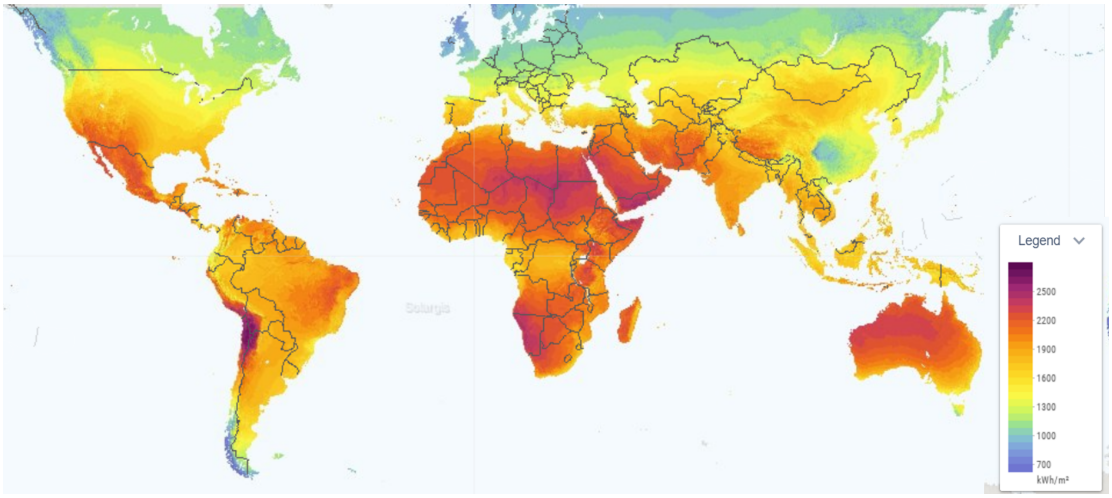

Figure 7: Global horizontal irradiation capacity

As shown in Figure 7, the annual horizontal solar radiation, incident on the earth's crust, places the solar energy as the most important renewable energy source. Some territories shows massive potential, still today unexploited [9].

Unfortunately, Concentrated Solar Power (CSP) deployment remains disappointing. On the other hand, in the last 15 years, solar photovoltaic energy has experienced an exponential global growth. As represented in Figure 8, solar PV generation has reached approximately 1.3 PWh, while CSP reached almost 12.8 TWh [10].

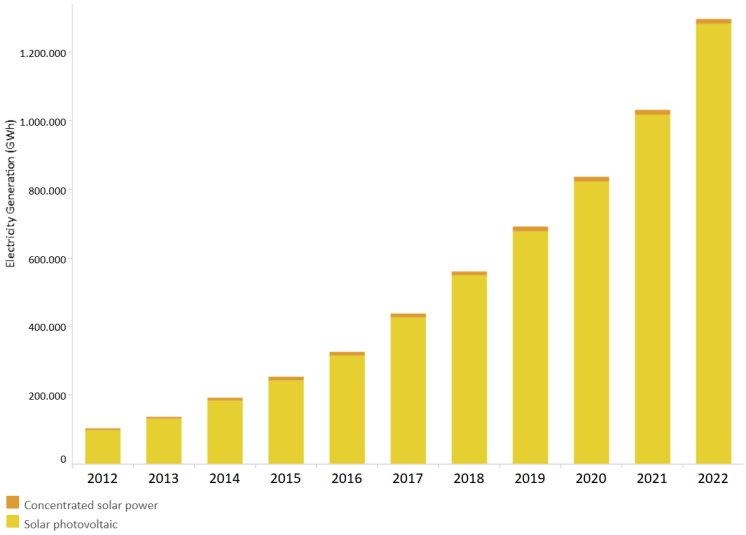

Figure 8: Electricity generation trend in GWh for Solar Energy from 2011 to 2022

One of the main advantages of a CSP power plant over a solar PV power plant is that it can be equipped with Thermal Energy Storage (TES) in which heat can be stored, allowing electricity to be generated after the sun has set. As

the CSP market has matured, one of the significant advancements has been the decline in the cost of thermal energy storage systems. This reduction in cost has made it economically viable for CSP plants to store energy for up to 12 hours, significantly increasing the storage duration and enhancing the flexibility of CSP plants. Furthermore, the ability to store heat and produce electricity during off-sunlight hours gives CSP systems a distinct edge in integrating higher shares of variable renewable energy sources, such as solar PV and wind power, into the grid. Since both wind and solar PV can fluctuate based on weather conditions, having a dispatchable power source like CSP, with its long-duration thermal energy storage, can help stabilize the grid and ensure a reliable supply of electricity, even when other renewable sources are intermittent. Thus, while CSP has often been underappreciated in the renewable energy conversation, its growing role could become increasingly important in the future energy landscape. With low-cost thermal energy storage, CSP not only complements other renewable sources but could also play a critical role in enabling a more sustainable and reliable energy system, allowing for greater integration of variable renewables while ensuring that energy supply remains constant and flexible.

In addition, according to the International Energy Agency (IEA), heating is the largest consumer of energy, representing about half of the total energy used for various purposes such as warming homes, industrial processes, and other applications. One potential approach to decarbonize Industrial Process Heat (IPH) systems is to boost electrification using available renewable energy sources. Another concrete option is to directly generate IPH through solar thermal technologies as CSP, especially for high temperature applications, placing CSP technology as one of the most versatile renewable energy sources.

Concentrated Solar Power (CSP) systems use mirrors or lenses to direct and concentrate sunlight onto a specific point or line. This concentrated solar energy is absorbed by a receiver, which usually contains a fluid that gets heated by the focused sunlight. The heat from the fluid is transferred to a working fluid, typically through a heat exchanger, where it is used to create steam. The steam is then sent to a turbine for generating electricity, which is then delivered to the electrical grid for use. Alternatively, the generated heat could be useful to directly run any IPH systems. Thus, any CSP systems can be projected and worked in hybrid mode, depending on the final end of use or on the location which is installed.

The simplified schematic of a Concentrated Solar Power (CSP) plant architecture, described in Figure 9 consists of three key subsystems [11]:

- **Solar Field**: It collects solar energy through mirrors or lenses that focus sunlight onto a receiver where flows the heat transfer fluid (HTF), used to transport the heat energy to the next components of the system.

- **Thermal Storage (TES)**: This unit stores the heat captured by the solar field. The primary and secondary subsystem could be operated with the same fluid (usually molten salts), to spare one heat exchanger, and to help in improving the efficiency and in reducing the operational complexity of the system.

- **Power Block or IPH block**: The stored thermal energy is transferred to

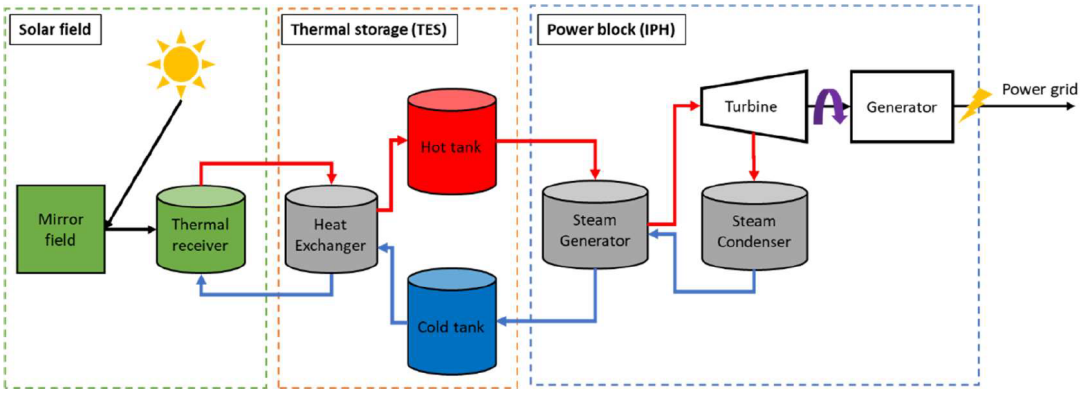

Figure 9: Schematic diagram of a CSP power plant

the power block, where it is used to generate electricity. This is typically done by heating water to produce steam, which drives a turbine connected to a generator. Alternatively the power block is substituted by an IPH system.

The diagram does not include any auxiliary heating sources that might be used to support or hybridize the system for guaranteeing an increased overall system reliability and efficiency.

CSP is typically deployed in large-scale power plants due to the high energy capacity and space requirements. These power plants are designed to harness the full potential of the sun's heat.

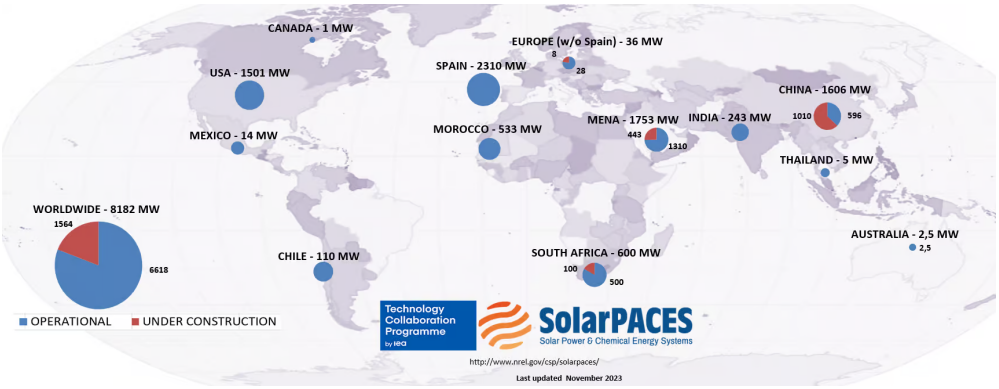

Figure 10: CSP world capacity

CSP applications are currently placed in approximately 20 countries, with an intermittent deployment since 1980_s. The global installed CSP capacity is 8.1 GW, 6.6 GW of operational capacity, and another 1.5 GW under construction, as represented in Figure 10 [12].

Spain and the United States are the counties with the highest CSP energy capacity, closely followed by the United Arab Emirates and China.

However, according to current patterns, China is positioned to take the lead in both CSP deployment and supply chain capabilities by the end of the decade. China has commissioned 40 new CSP projects under various stages of construction, more than 1 GW, and commissioning, around 3 GW [13].

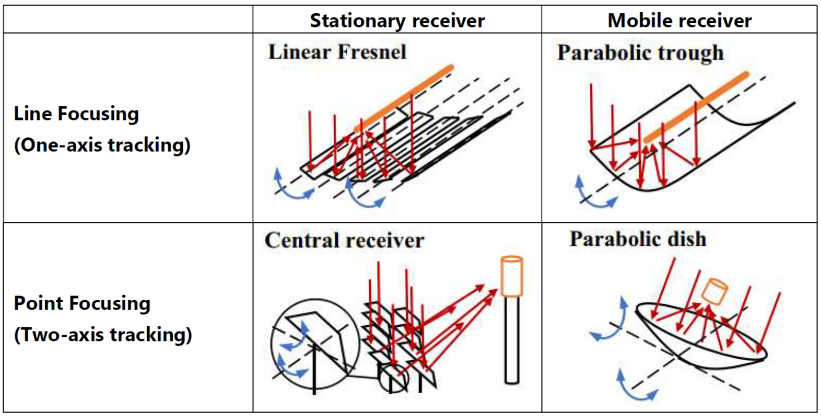

Figure 11: Overview of main CSP configurations

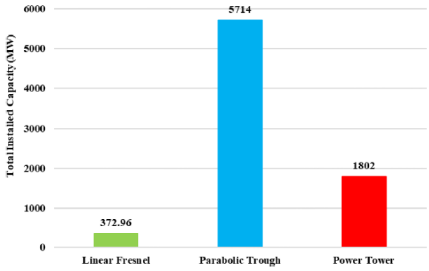

Figure 12: CSP configurations share

There are two types of concentration technologies, line or point focusing. Point-focusing systems, such as Solar Power Tower and Dish Stirling, concentrate solar energy onto a single point using precisely oriented mirrors, such as heliostats or paraboloidal dishes.

As represented in Figure 12, Dish Stirling is not taken into consideration because is not so spread and considered as a small-scale application.

Instead, Power Tower technology is more spread and applied at large scale. Its massive size allows for high temperatures, typically between 500 °C and 1000 °C, making these systems ideal for advanced applications like high-efficiency power generation [14].

On the other hand, their design complexity, the need for precise solar tracking, and significantly massive costs restrict their use to niche projects.

In contrast, the line-focusing configuration is not able to reach certain ranges of temperature and efficiency due to the lower energy density; nevertheless, it is characterized by a simpler design and relatively lower installation costs making it an economic and viable solution for medium-temperature applications on an industrial scale.

LFC and PTC configurations

Line-focusing CSP technology encompasses Linear Fresnel Collector (LFC) and Parabolic Trough Collector (PTC), the most widespread of the two. LFC system comprises multiple parallel strips of flat or slightly curved lens, while PTC is composed by parallel rows of parabolic mirros. Both of them concentrate the incident solar radiation onto a receiver line, usually for LFC is singular for the entire system, while, PTC presents a focus line for every rows [15].

Figure 13: PTC configuration - LFC configuration

The receiver unit consists in a metallic absorber tube usually encapsulated in a glass envelope, to reduce both convective and radiative thermal losses. Furthermore, it may be evacuated or not.

The evacuated configuration, with vacuum between the absorber tube and the glass (10^2 Pa), obviously provides higher impact on life cycle costs.

On the other hand, it allows to reduce the convective heat transfer and to preserve the selective coating of the absorber tube from high temperatures, due to the fact that the stability of the absorber tube coating, in certain conditions, is still under debate.

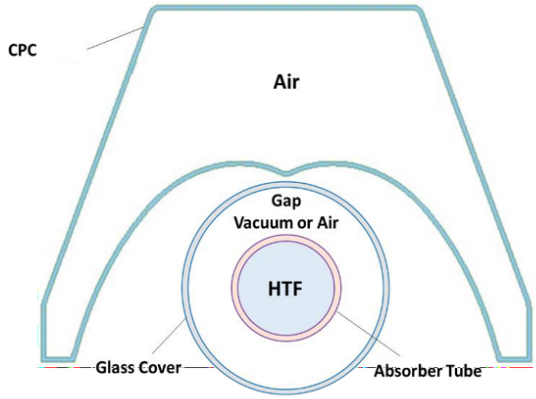

Figure 14: LFC configuration design with CPC

Furthermore, as shown in Figure 14, LFC also adopts a secondary concentrator, CPC (Compound Parabolic Concentrator), mounted above the receiver, which allows to reconcentrate the solar radiation that is not captured by the absorber tube.

Moreover, its frame is able to improve the insulation performance of the receiver unit, thus consequently, to lower the convective heat losses and to increase the thermal efficiency.

The CPC (Compound Parabolic Concentrator) is usually a trapezoidal metallic frame filled with air at atmospheric pressure. It is usually composed by materials with high reflectivity, for diverting incident radiation.

On the other hand, the absorber tube is usually coated by selective materials

allowing for high absorbivity and low emissivity, to insulate the heat in the focal line of the receiver unit.

In general, LFC is presenting as simpler designed and more cost-sustainable than PTC, indeed with CPC introduction, it performs better than the parabolic trough in terms of receiver thermal efficiency.

In contrast, the LFC configurations are not so optically efficient and that is the main reason explaining their lower overall energy yield compared to PTC. Innovative LFC layouts have been proposed with the aim to overcome the gap in optical efficiency compared with PTC; as for example in [16].

It is also worth mentioning that LFC is a less mature technology, and generally, presents more margins because of lower capital costs that allows more flexibility in terms of usage of new type of materials, or different layouts, enabling improvements in term of performances, hopefully in the not too distant future [17], [18].

In particular, the present project, leveraging on the more flexible scenario around the LFC, puts attention on the thermal enhancement given by the usage of CPC on the receiver unit. Technical studies, performed via CFD on $STARCCM+$, are going to demonstrate the utility of the CPC frame and to make an overall evaluation of the impact it makes on the receiver unit of a LFC system.

CSP efficiency

The Carnot efficiency sets the highest possible CSP efficiency according to the laws of thermodynamics. This is a theoretical limit, meaning that no real-world system exceeds it. It represents the best-case scenario for energy conversion, in fact, practical systems always experience losses due to several factors.

By reaching higher operating temperature levels, the efficiency of the thermodynamic cycle can be increased, as described by Eq. 1.

$$\eta_{\text{sys}} < \eta_{\text{Carnot}} = 1 - \frac{T_{\text{cold}}}{T_{\text{hot}}} \tag{1}$$

T_{cold} and T_{hot} respectively represent the inlet and outlet temperatures of the heat transfer fluid, in Kelvin.

The overall efficiency of a CSP system is the final aggregation of several parameters , as following [14]:

$$\eta = \eta_{\text{optical}} \cdot \eta_{\text{receiver}} \cdot \eta_{\text{mechanical}} \cdot \eta_{\text{generator}} \tag{2}$$

- η_{optical} represents the fraction of incident sunlight that is concentrated onto the receiver.
- η_{receiver} is the fraction of the concentrated sunlight that is absorbed and converted into heat energy by the receiver.
- $\eta_{\text{mechanical}}$ indicates the efficiency with which the heat energy is converted into mechanical energy; is at most the Carnot efficiency.
- $\eta_{\text{generator}}$ represents the efficiency of converting mechanical energy into electrical power.

η_{optical} is directly affected by the Concentration Ratio C_x of the system. C_x is the ratio of the mirror aperture area respect to the receiver area.

$$C_x = \frac{A_a}{A_r} \tag{3}$$

Point focusing systems achieve a higher geometric concentration ratio in comparison to line focusing ones. Higher C_x values allow to achieve higher operating temperature levels, which is beneficial for improving efficiency. However, this comes with the trade-off of needing more advanced and precise optical components. The concentrator and tracking systems, in particular, must be much more accurate to maintain the correct alignment and focus the sunlight on the receiver.

$$\eta_{\text{receiver}} = \frac{Q_{\text{absorbed}} - Q_{\text{lost}}}{Q_{\text{incident}}} \tag{4}$$

where:

- Q_{incident} represents the incoming solar flux.
- Q_{absorbed} represents the flux absorbed by the receive.
- Q_{lost} represents the flux lost by the system.

$$Q_{\text{solar}} = IC_xA_r \tag{5}$$

$$Q_{\text{incident}} = \eta_{\text{opt}}Q_{\text{solar}} \tag{6}$$

$$Q_{\text{absorbed}} = \eta_{\text{opt}}\alpha Q_{\text{solar}} \tag{7}$$

$$Q_{\text{lost}} = A_r\epsilon\sigma T^4 \tag{8}$$

Theoretically, Point Focusing Collectors (PFCs) are able to reach higher temperature, in some applications more than 1000 °C, thus, are able to provide higher efficiencies, up to 35%. Usually line focusing collectors achieve smaller value of efficiency, typically <=20% [14].

Heat transfer fluid

Before has been seen the role of the heat transfer fluid (HTF) to guarantee the higher possible level of efficiency, just adjusting the working temperature.

On the other hand, the temperature is not the only parameter to be considered, in fact, CSP systems may use several heat transfer fluids, depending on the scope of the application, on environmental constraints, or simply on the availability of materials.

In the current project, a LFC system is considered; computations are performed in a wide T range (200-500 °C), giving an all around outlook on the heat transfer fluids which can be used in the system:

- **Molten Salt Mixture (60%wt. $NaNO_3$ + 40%wt. KNO_3)**: $290 - 500$ °C

  It is typically used for medium to high-temperature CSP systems.

  Advantages:

  - High specific heat capacity, which allows to store large amounts of thermal energy.
  - Used for thermal energy storage over long periods, making it ideal for the dispatchment.

  Limitations:

  - Molten salts freeze at temperatures 220 °C, requiring heating systems to ensure they remain in a liquid state when temperatures drop.
  - Corrosive nature. It may be prevented selecting the right materials (high-performance alloys), ensuring purity and temperature control, and using coatings, inhibitors, and maintenance practices to reduce corrosion risks.

- **Therminol VP-1**: 290 – 400 °C

  Synthetic oil typically used for medium-temperature CSP systems.

  Advantages:

  - Stable and has good thermal stability over long periods of use.
  - Low viscosity

  Limitations:

  - It is not suitable for very high-temperature CSP systems (above 400 °C).
  - Relatively low specific heat capacity compared to molten salts, thus, it is not used for thermal storage applications.

- **DelcoTerm Solar E15**: 200 – 300 °C

  Paraffinic oil operating in lower temperature range of CSP systems, making it suitable for smaller-scale systems or regions with lower solar intensity.

  Advantages:

  - Good thermal stability.
  - High flash point, low vapor pressure, absolute chemical inertia towards all materials used in the thermic circuits.
  - Resistant to common deterioration phenomena such as oxidation and cracking

  Limitations:

  - The maximum temperature of 300 °C limits its applicability to low-temperature CSP systems.
  - Low specific heat capacity compared to molten salts.

Preliminary study

Development of the CFD Model

This chapter talks about a simple Computational Fluid Dynamics (CFD) model performed on a singular cylinder in cross flow, simulating the receiver tube of a LFC or a PTC system. CFD modelling allows of solving, numerically, the dynamic mass, momentum and energy balance equations for fluid regions, reproducing properly the fluid flow and the heat.

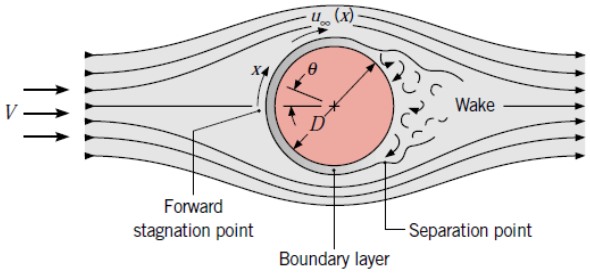

Figure 15: Cylinder in cross flow

In addition, it solves energy conservation heat transfer equations at interfaces, by subdividing the domain into a finite number of smaller control volumes (CVs), while the physical time is discretised in a finite number of time steps.

Thus, CFD analysis offers significant advantages by providing highly accurate simulations of experiments at a lower cost compared to physical testing. However, the main drawback could be that running these simulations requires substantial computational power, which can be expensive and time-consuming.

The model is simulating the receiver unit, taking into account several simplifications and hypothesis. The axial dimension is neglected, overlooking the heat transfer flux along the receiver axis direction; thus the system is evaluated in two dimensions (receiver cross section) with the aim to calculate the heat transfer in the radial direction, as shown in figure 16.

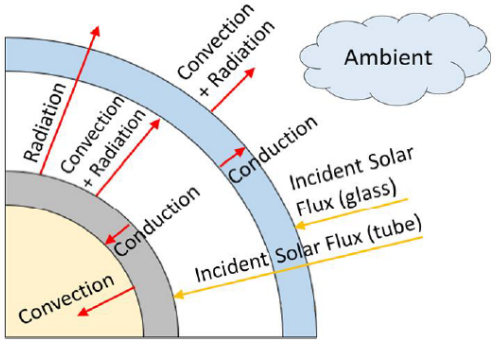

Figure 16: Heat fluxes along the cylinder radial direction

The preliminary CFD model, implemented on $STARCCM+$, is even more simplified with respect to the previous figure. The external surface (glass) is considered as the only reference heat transfer surface, and thus the receiver unit as a unique entity.

Furthermore, due to low thickness, the conduction phenomena is disregarded and so heat losses are encompassing only the convection and radiation share.

The computational domain is formed by the external air, but does not foresee the CPC shell.

In the "*Continua*" section, air is considered as an ideal gas at 300 K, presenting the following characteristics:

- Temperature: 300 (K)
- Conductivity: 0.0263 $(W/m\mathring{u}K)$
- Dynamic Viscosity: 1.85e-5 $(Pa\mathring{u}s)$
- Prandtl: 0.707
- Specific Heat: 1007 $(J/kg\mathring{u}K)$
- Density: 1.086 (kg/m^3)

The model is implemented with the following main conditions:

- Steady State
- Coupled Flow
- Coupled Energy
- K-ϵ Turbolence
- Ideal Gas
- Gravity

The coupled solver implements all the governing equations simultaneously, within each iteration. It is more accurate and ensures a faster convergence with respect to segregated conditions.

Instead, K-ϵ turbulence model uses Reynolds-averaged Navier-Stokes equations for simulating turbulence in fluid flows. it is widely used with high Reynolds numbers, demonstrating of being more simple and robust with air flows.

Indeed, it features low computational cost, that, in the case of a preliminary study, is a key parameter.

The analysis is performed calculating the heat transfer between the cylinder and the external air. Heat motion is driven by the static temperature boundary condition, on the outer surface of the cylinder.

Independence mesh study is performed to assess the reliability of the meshing design and to ensure the accuracy of results.

In fact, Wall $Y+$ is an evaluated parameter calculated to verify the correct behavior of the system around the boundary layers by simulating the correct flowing of the fluid. It is another evaluation factor for guaranteeing the accuracy of the mesh design.

Wall $Y+$ is a dimensionless parameter describing the non-dimensional wall distance in turbulence modeling, particularly the behavior of flows in boundary regions, relative to the mesh scene.

$$Y^{+} = \frac{y \cdot u_{\tau}}{\nu} \tag{9}$$

Wall $Y+$ represents how far a point in the mesh is from the wall, relative to the viscous layer of the flow. If Wall $Y+ < 1$, it means that the meshing cell is within the viscous layer. In this region, the flow is dominated by viscous forces, and the turbulence model demonstrates to be very accurate near the wall. Where:

- y distance from the wall (m)
- u_{τ} wall shear velocity (m/s)
- ν kinematic viscosity (m^2/s)

Natural Convection

The first analysis is done on a restricted squared domain, where the receiver unit, placed in the center, presents a fixed temperature along the external perimeter. As shown in Figure 17, the squared domain is 0.8 m * 0.8 m, with cylinder diameter equal to 125 mm.

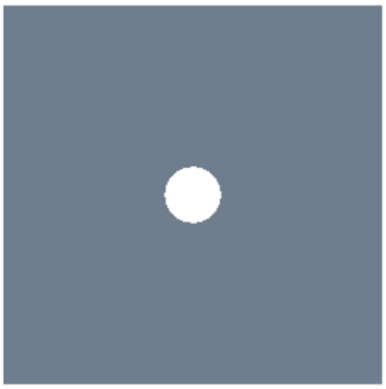

Figure 17: Geometry of natural convection model

Both the right and left sides of the domain are set on a "symmetry plane" condition, while the upper part on "pressure outlet". The bottom side and the cylinder itself are set on "wall" condition.

The mesh, implemented as in the Figure 18, is well-discretized, in fact, it presents a Wall $Y+$ on the cylinder of 0.1.

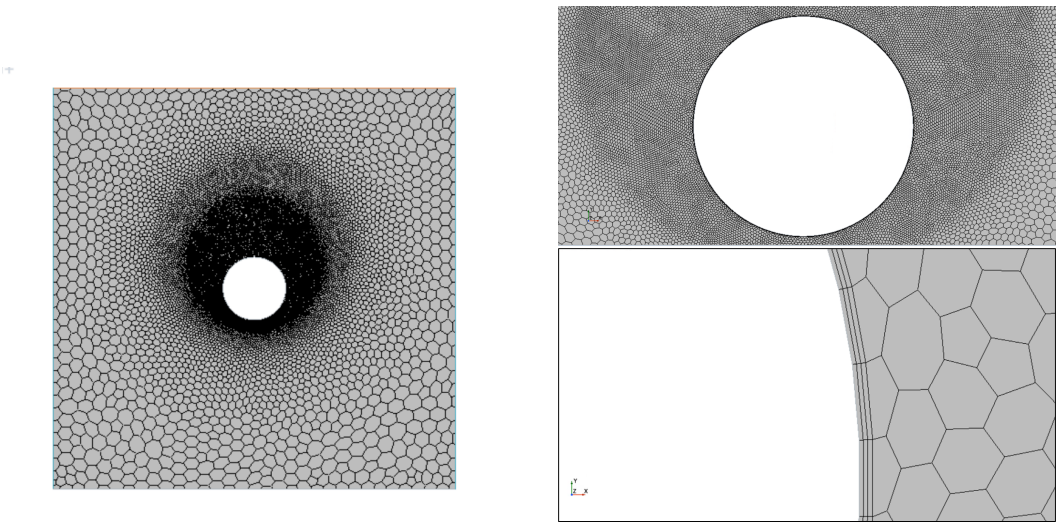

Figure 18: Meshing of natural convection model

It is the result of "$Automated2DMesh$" implemented with polygonal and prism layer mesher. Prism layers, as shown in 18, are three, with a total number of cells equal to $3 * 10^4$. The characteristics of the chosen mesh are the following:

- Base Size = 0.01 m
- Surface Growth Rate = 1.1
- Target Surface Size = 100%
- Minimum Surface Size = 10%
- Number of Prism Layers = 3
- Prism Layer Stretching = 1.01
- Prism Layer Thickness = 5e-4 m

	Mesh 1	**Mesh 2**	**Mesh 3**
N°cells	33400	55284	118390
Q (W/m)	270.4	266.2	277.5
NU	26.9	26.5	27.5
Wall Y+	0.1		

Table 2: Independence mesh study natural convection model

The independence mesh study certifies the choice of the current mesh design. Tripling the number of cells does not cause a massive variation, around 2.5% for Q and 2.2% for Nu. Thus to avoid a higher computational time, the chosen mesh design is the perfect trade-off between accuracy and time consuming [19].

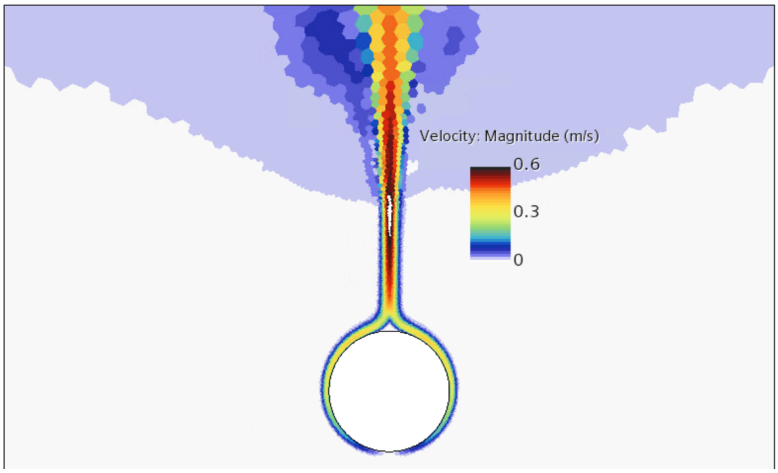

Figure 19: Velocity field of natural convection model

Regarding the temperature field, the external air temperature is set at 300 K and, in this case, the cylinder one at 423.15 K. The convection is naturally driven and is not perturbed by any kind of external source

Figure 19 suggests how the natural convection, driven by temperature and pressure gradients, is able to create a natural velocity field, in absence of wind [20].

It is possible to notice the direct correlations between temperature and velocity fields, as shown in both Figure 19, 20.

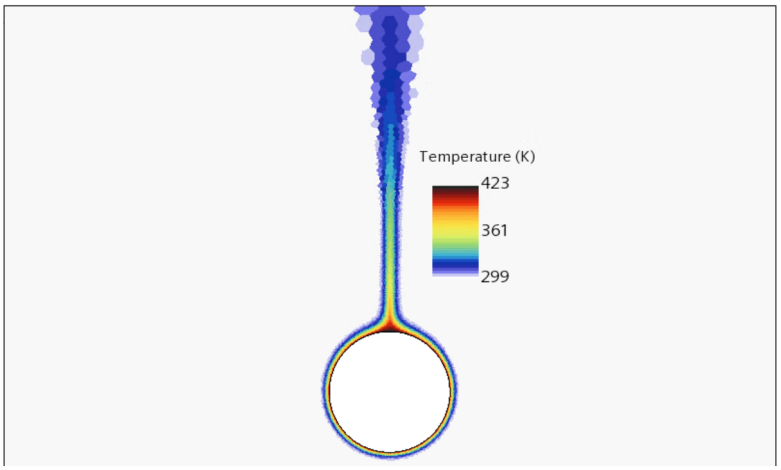

Figure 20: Temperature field of natural convection model 423 K

The Figure 20 underlines how the temperature field, distributed along the cylinder perimeter, is affected by the pressure which is acting on the top of the domain. It is possible to notice that, on the back of the cylinder, the isothermal areas are wider and there is a bigger surface where T is equal to 423 K, the peak temperature, as well as the static temperature applied in the "*Boundaries*" of the cylinder.

After calculating the heat transfer on the cylinder Q, equal to 270.4 (W/m), is possible to obtain h, convective heat transfer coefficient $(W/m^2 \mathring{u} K)$, following Eq.10.

$$Q = h \cdot A_{\text{dome}} \cdot (T_{\text{dome}} - T_{\text{amb}}) \tag{10}$$

Once h is determined, the Nusselt number Nu_D can be obtained by Eq.11.

$$Nu_D = h \cdot \frac{D}{k} \tag{11}$$

Where:

- D = cylinder diameter (m)
- k = thermal conductivity of the fluid $(W/m \mathring{u} K)$

Nu_D is a dimensionless quantity related to the effectiveness of convection, compared to the rate of heat transfer by conduction alone. A higher Nusselt number indicates that convection is playing a more significant role in the heat transfer process.

Thus, the results of the CFD model, obtained through the switch of temperature on the cylinder surface, as shown in Figure 21, are compared with the correlations provided by Churchill and Chu. (Eq.12) and Morgan (Eq.13)[21].

$$Nu = \left(0.6 + \frac{0.387 \cdot \left({Ra_D}^{1/6} \right)}{\left(1 + \left(\frac{0.559}{Pr} \right)^{9/16} \right)^{8/27}} \right)^2 \tag{12}$$

$$\bar{N}u_D = C \cdot Ra_D^n \tag{13}$$

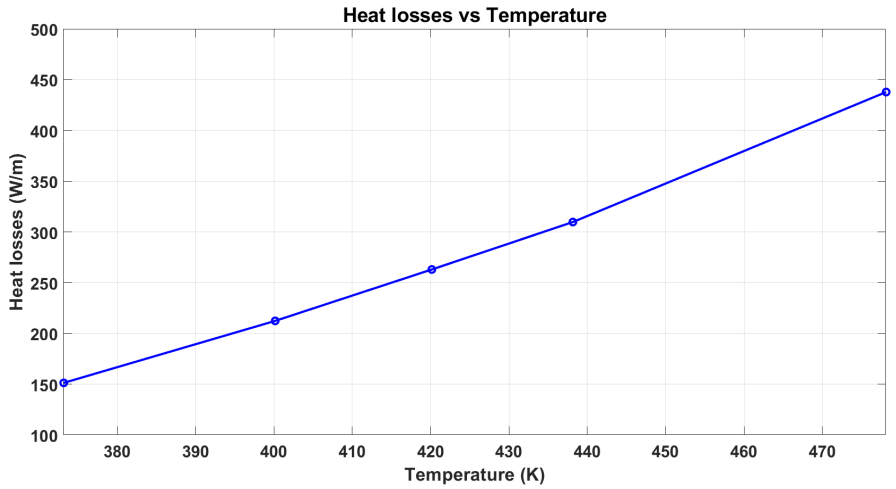

Figure 21: Heat losses vs. Temperature natural convection model

The properties are evaluated at $Tfilm$; Ra_D represents the Rayleigh number for air, based on the glass envelope outer diameter, Pr is the Prandtl number for air at film temperature, C and n are given in [21].

Pr is a dimensionless parameter that describes the ratio of momentum diffusivity (kinematic viscosity) to thermal diffusivity in a fluid. In this work, it is obtained by tables in [21].

Instead, Ra_D is a dimensionless number that combines the effects of thermal convection and viscosity of the fluid. It is used to determine the flow regime in natural motion conditions, Eq.14.

$$Ra_D = \frac{g\,\beta\,(T_s - T_\infty)D^3}{\nu\,\alpha} \tag{14}$$

Where:

- g = gravitational acceleration (m/s^2)
- β = thermal expansion coefficient of the fluid $(1/K)$
- T_s = temperature of the surface (K)
- T_∞ = temperature of the surrounding fluid (K)
- D = cylinder diameter (m)
- ν = kinematic viscosity of the fluid (m^2/s)
- α = thermal diffusivity of the fluid (m^2/s)

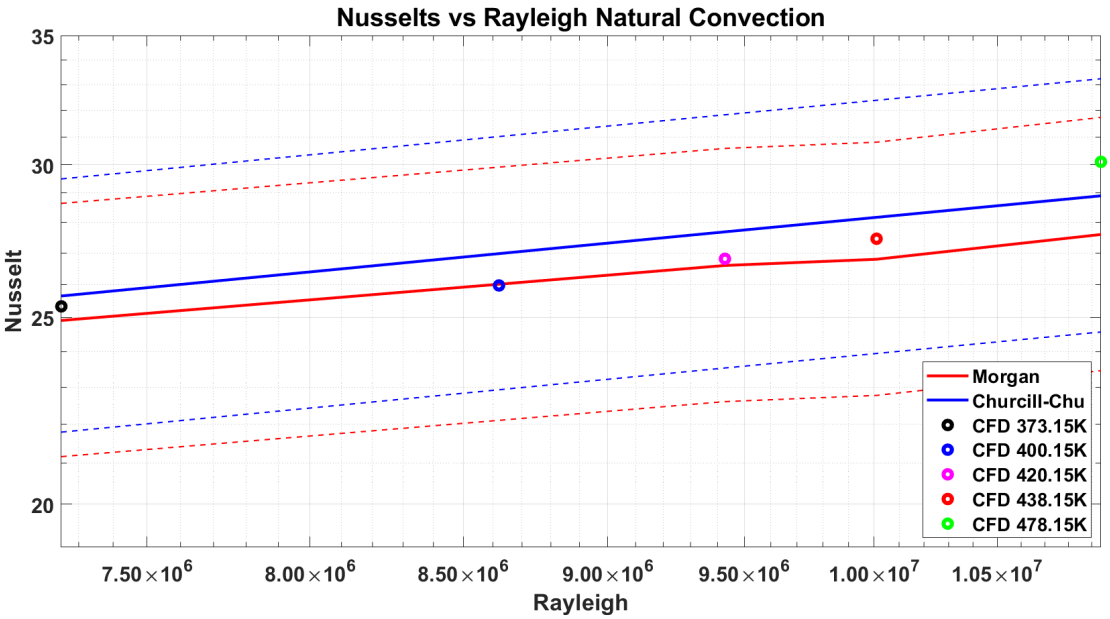

Figure 22: Nusselt vs. Rayleigh natural convection model

The Figure 22 shows that the Nusselt numbers, predicted by the CFD model, match the values obtained from Churchill and Chu. and Morgan correlations.

The comparison is made across a range of Rayleigh numbers, changing the fixed temperature on the cylinder. As Eq. 14 shows, increasing the superficial temperature, Ra_D increases too. Nu_D due to the raise of the temperature gradient is more affected by the convective heat transfer.

Considering an upper and lower tolerance of 15%, the observed maximum deviation corresponds to 4.2%, confirming the reliability of the current analysis and of the CFD model.

Forced Convection

The forced convection model differs from the natural convection one because of the presence, on the left side of the computational domain, of an imposed transversal wind speed. On the opposite side, a "pressure outlet" boundary condition is applied to set the ambient pressure at the right of the control volume. The wind speed in the "velocity inlet" boundary condition is set in the range (2-10 m/s).

Figure 23: Geometry of forced convection model

The domain, as shown in Figure 23, is larger, 3 m * 4.5 m, with the same cylinder diameter and a Wall $Y+$ value around 0.15, ensuring the reliability of the mesh around boundary layers of the cylinder.

The models used in the "*Continua*" section are the same as the natural convection design, but the mesh scene, shown in Figure 24, underlines the following characteristics:

- Base Size = 0.02 m
- Surface Growth Rate = 1.1
- Target Surface Size = 100%
- Minimum Surface Size = 10%
- Number of Prism Layers = (2 - 6)
- Prism Layer Stretching = 1.01
- Prism Layer Thickness = 1e-4 m

The total cells ensuring the independence of the mesh are 8.7 * 10^5, with a variable number of prism layers, proportional to the increase of the wind velocity from the left, to maintain Wall $Y+$ almost constant.

Wind speed (m/s)	2	3	4	5	6	7	8	9	10
Prism layers	2	2	3	3	4	4	5	6	6
Wall Y+	0.15								

Table 3: Number of prism layers forced convection model

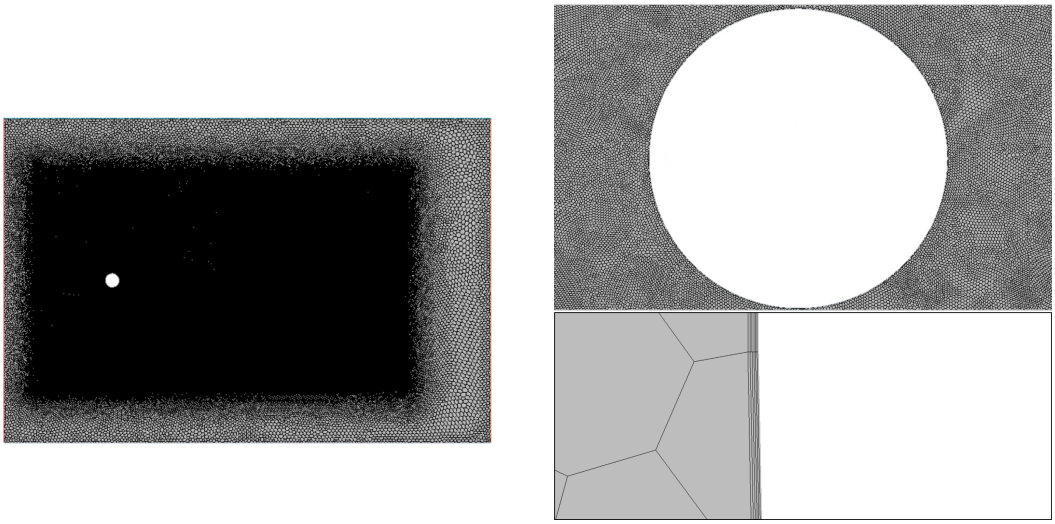

Figure 24: Meshing of forced convection model

The current meshing is a satisfactory trade-off between the accuracy and the computational cost, which both increase with the number of the cells in the mesh [19].

	Mesh 1	**Mesh 2**
N°cells	875465	1731721
Q (W/m)	1665	1693
NU	201.7	205.2
Wall Y+	0.15	0.11

Table 4: Independence mesh study forced convection model 10 m/s

Doubling the number of cells, variations of significant values are almost inconsequential, around 1.5% for Nu_D and Q, justifying the choice of the current mesh layout.

Moreover, the receiver unit is not placed at the center of the domain but closer to the wind inlet section (left). This positioning ensures that the vortices generated downstream of the receiver unit are fully captured and resolved within the control volume, preventing them from exiting before being properly analyzed, as represented in Figure 25.

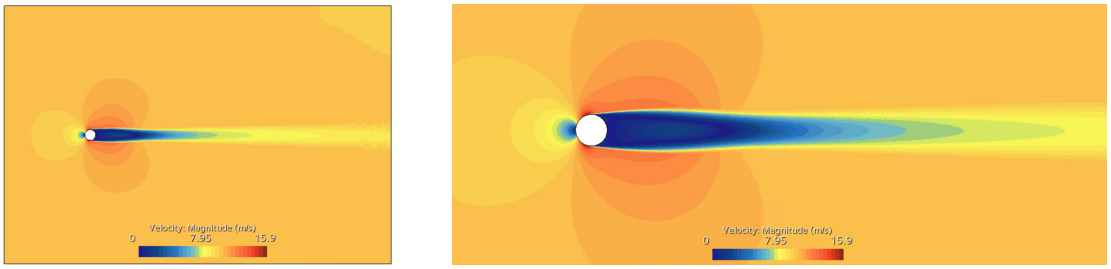

Figure 25: Velocity field forced convection model 10 m/s

The current analysis is done taking into consideration the CFD simulation where wind speed applied on the left side is $10m/s$.

However, in Figure 26, it is possible to visualize higher values around the cylinder, due to the constructive interference.

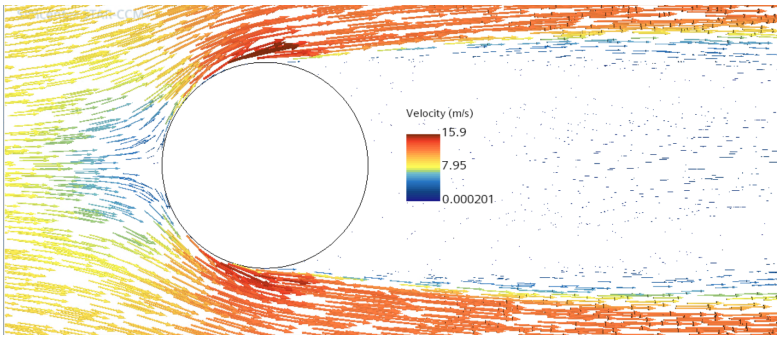

Figure 26: Vector field of velocity forced convection model 10m/s

Vector constructive interference is a phenomenon that occurs when two or more vectors combine in such a way that the resulting vector has a greater magnitude than the individual vectors. This happens when the vectors are oriented in directions that favor a positive algebraic sum of their components.

Regarding the T-field analysis, as shown in Figure 27, the temperature gradient, $\frac{\partial T}{\partial x}$, on the back of the cylinder, is smaller than the one on the front, due to the wind blowing from the left.

Furthermore, because of higher heat transfer amount, the temperature field around the receiver unit is thinner than the one in the natural convection model, and the maximum peak temperature, $400K$, is less spread along the cylinder [20].

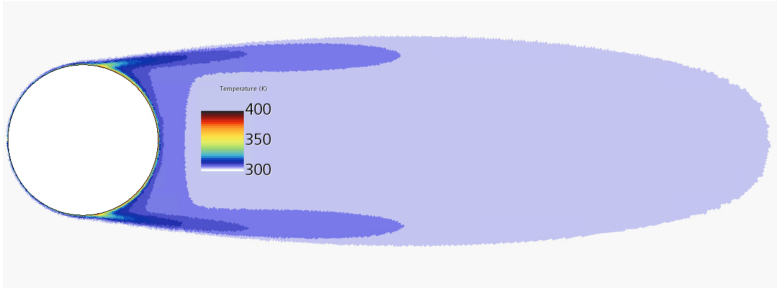

Figure 27: Temperature field forced convection model 400 K

The heat losses present an almost linear behavior with respect to the increase of velocity. Obviously, more wind speed means more convective motion, thus, a higher convective heat transfer coefficient h, thus, higher losses, as Figure 28 shows.

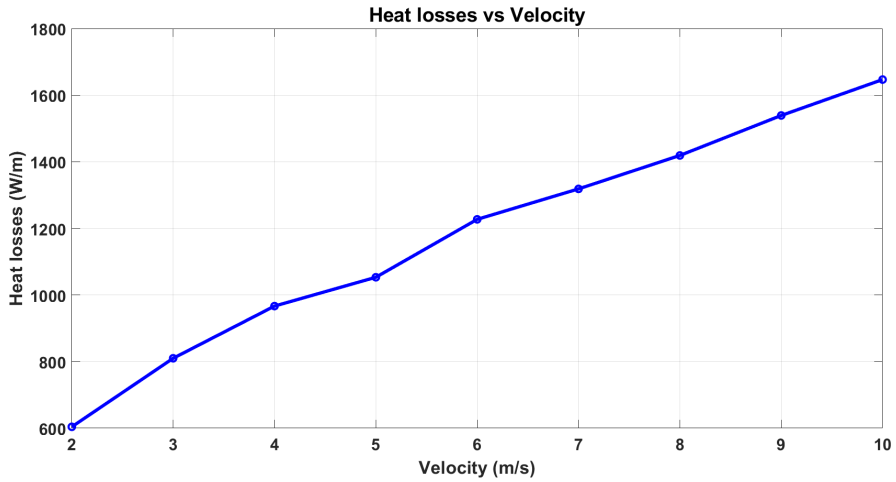

Figure 28: Heat losses vs. Velocity forced convection model 400 K

Similar to natural convection, the forced convection model is first validated using a well-known correlation, from the literature for a cylinder in crossflow, without the CPC [21]. In particular, Zhukauskas correlation is applied, as shown in Eq.15.

$$Nu = C \cdot Re_D^m \cdot Pr_{atm}^n \cdot \left(\frac{Pr_{atm}}{Pr_{glass}}\right)^{\frac{1}{4}} \tag{15}$$

All properties are evaluated at T_∞ and in the current range: [0.7<Pr<500], [1<Re_D<10e6]. Re_D represents the Reynolds number based on the outer diameter of the glass envelope, while Pr_a and Pr_g are the Prandtl numbers evaluated at the atmospheric and glass temperatures, respectively. The coefficients C, m, and n are defined in [21] as functions of the Reynolds and Prandtl numbers.

Re_D is a dimensionless number that outlines the flow regime of a fluid (whether it is laminar or turbulent). It is given by Eq. 16:

$$Re_D = \frac{\rho u D}{\mu} \tag{16}$$

Where:

- ρ = density of the fluid (kg/m^3)
- u = velocity of the fluid (m/s)
- D = cylinder diameter (m)
- μ = dynamic viscosity of the fluid $(Pa \times s)$

The analysis is performed, increasing the velocity of the wind from the left side, and making Re_D to rise too. The enhancement of velocity around the cylinder influences positively the convective heat transfer, causing a gain in the Nusselt number values.

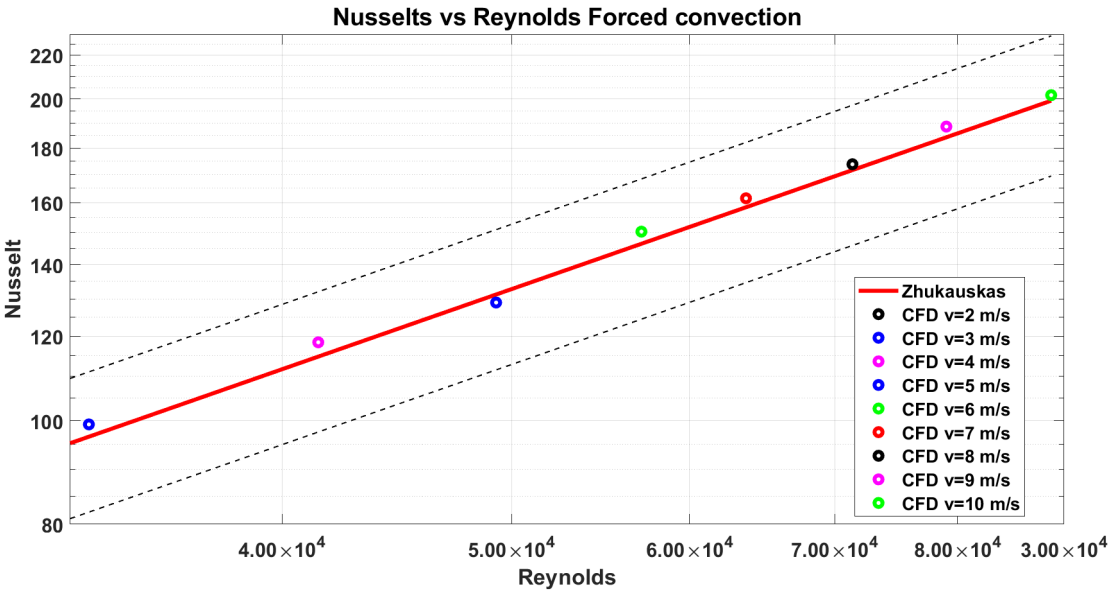

Figure 29: Nusselt vs. Reynolds forced convection model

The tolerance lines are fixed with a deviation of 15%, that as noted in [21], would be acceptable for most engineering calculations. As represented by Figure 29, the current CFD model calculations fall around the values obtained by Zhukauskas correlation, and within the tolerance range. In fact, the maximum registered deviation is 3.5%, manifesting the reliability of the CFD analysis.

Natural vs Forced Convection

In dealing with forced convection, the effects of free convection is usually ignored.

In reality, a portion of the convective motion should be carried out by the natural convection phenomena too. Thus it is correct to talk about mixed convection and not individually of forced and natural convection. As said in [21], to take into consideration the weight of free convection, it has become common practice to compare mixed external convection heat transfer results with the following Eq.17.

$$Nu_{\mathrm{n}}^{n} = Nu_{\mathrm{F}}^{n} \pm Nu_{\mathrm{N}}^{n} \tag{17}$$

Nu_F and Nu_N are obtained from existing correlations, respectively for forced and natural (free) convection. The plus sign is applied for assisting and transverse flows, while the minus sign applies for opposing ones.

$n = 4$ for cylinders in cross flow.

Thus, in the current study, the reference Nusselt number correlation is a mixing of the Churcill and Chu. and of the Zhukauskas correlation, as shown in Eq.18.

$$Nu_{\mathrm{tot}} = \left(\left(\text{Churcill-Chu}^4\right) + \left(\text{Zhukauskas}^4\right)\right)^{\frac{1}{4}} \tag{18}$$

Thus, combining these two, it is possible to calculate their relative share respect to the total heat transfer phenomena. Let's consider the heat transfer for the cylinder whose surface it is at 400 K.

	2 m/s	**3 m/s**	**4 m/s**	**5 m/s**	**6 m/s**	**7 m/s**	**8 m/s**	**9 m/s**	**10 m/s**
Forced	98.07%	99.26%	99.63%	99.78%	99.86%	99.9%	99.93%	99.94%	99.96%
Natural	1.93%	0.74%	0.37%	0.22%	0.14%	0.10%	0.07%	0.06%	0.04%

Table 5: Natural and forced relative share in mixed convection model

The free motion contribution is almost negligible, and increasing the wind speed, so the forced convection, its relative share decreases until becoming almost zero.

Taking apart the mixed convection analysis, let's now compare, individually, the natural and forced models, with respect to their losses Q and Nu_D, as follows.

	Natural	**2 m/s**	**3 m/s**	**4 m/s**	**5 m/s**	**6 m/s**	**7 m/s**	**8 m/s**	**9 m/s**	**10 m/s**
Q(W/m)	212.3	604.1	809.9	966.6	1053.2	1227.1	1318.5	1418.9	1538.9	1646.68
NU	25.97	74	99.2	118.4	129	150.3	161.5	173.8	188.5	201.7

Table 6: Nu numbers and heat losses for natural and forced convection models

In Tab.6, it is possible to notice how the wind speed impacts on the convection model. An ideal inconsequential wind speed of 2 m/s causes a three times greater increase of the current heat losses.

It is fair to say, that gaps between the velocity inlet wall and the cylinder, and between the cylinder and the pressure outlet, are different in the two domains, wider in the forced convection one. However, hypothetically considering same domain size, the underlined phenomena can only be more powerful.

CPC introduction

This chapter outlines the introduction of a new CPC (Compound Parabolic Concentrator) structure, in a new CFD domain which is designed to more accurately estimate the heat flux to the surrounding environment.

The scope of CPC is primarily related to improve the efficiency of the solar energy collection process. Its frame is able to insulate the receiver unit and to reconcentrate solar radiation onto the absorbed tube.

LFC systems, as said previously in the "Introduction" section, suffer from optical losses because of the presence of a singular receiver unit for the entire Fresnel lens field. Optical losses are typically associated with conventional systems where sunlight might miss the receiver. The CPC introduction ensures more sunlight is captured and directed accurately onto the receiver, even when the sun's position is not optimal, resulting in a global increase of optical efficiency.

The new CFD system, using 2D steady-state model, is simulating the interaction between the external airflow and the inner part of the CPC frame, where the absorber tube or a block of smaller tubes should be.

Incorporating both convection and radiation contributions and varying wind conditions, the system is able to compute the heat transfer on the inner surface of the secondary concentrator, at different temperature.

The influence of CPC on the model is strongly dependent on its geometry. As shown in 30, the acceptance angle and the truncation origin are fundamental parameters, for making the system able to extract as much sun light as possible [18]. Obviously, the internal and external radius are crucial factors, but, in the current project, the absorber tube/tubes is not taken into consideration.

The new CFD model is described in next sections.

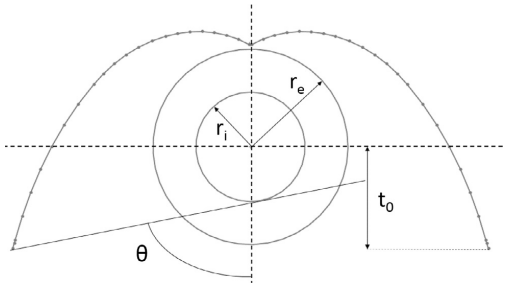

Figure 30: Setting of the CPC profile

Parameter	Symbol
Absorber tube ext radius	r_i
Glass cover ext radius	r_e
Acceptance angle	θ
Truncation origin	t_o

Domain of the CPC model

The domain, as shown in Figure 31, is similar to the forced convection one, a bit larger, 3 m * 5.5 m, for ensuring that all simulations and scenarios are solved within it.

2D DOMAIN:

- X coordinates: [-1 m, 4.5 m];
- Y coordinates: [-1.5 m , 1.5 m].

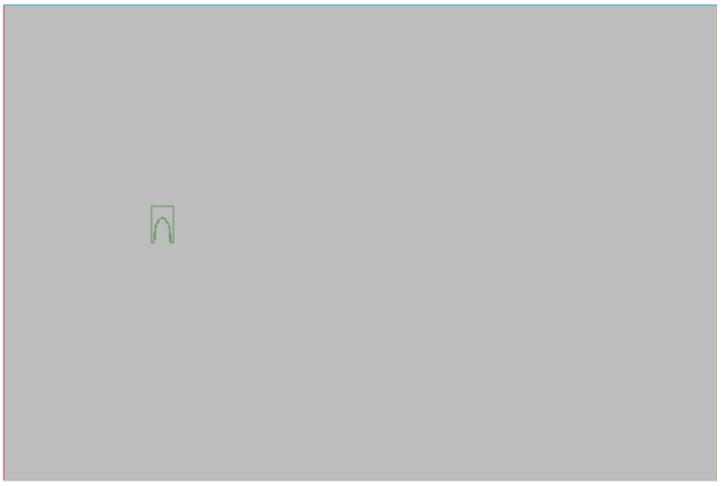

Figure 31: Domain with CPC introduction

Differently from the preliminary study, where the domain is composed by a unique entity, the new model encompasses three different components:

- **External air**
- **CPC air**
- **CPC frame**

They are imported on $STAR-CCM+$, after being designed on $SOLIDWORKS$, making them suitable for composing a final aggregated body. Each component is stuck in the other, creating interfaces from surfaces in contact.

The model is able to compute thermal heat losses, considering both radiation and convection contributions. Thus, radiation it is introduced and plays a strong influence on new calculations.

As can be noticed, the new domain does not include the absorber tube, usually set in the cavity of the CPC frame. Its role is replaced and simulated by the upper cavity of the internal frame, set at different temperatures and able to drive the heat transfer throughout the system.

External air

Figure 32: External air domain

The Figure 32 represents the 3D CAD model imported on $STAR-CCM+$, before being subjected to a 2D meshing operation.

The temperature at which the external air is set is 300 K.

- **Material:** Air (Ideal Gas)
- **Density:** 1.086 (kg/m^3)
- **Conductivity:** 0.026 (W/mK)
- **Specific Heat:** 1003.6 (J/kgK)

The applied boundary conditions on the current body are the same of forced convection model. The "velocity inlet" on the left side simulates the wind presence, which is developed in the range from 2 to 10 m/s.

On the other side, the "pressure outlet" condition makes the velocity wake able to develop at the right side of the CPC frame.

The bottom part of the domain is set at "wall" condition, while the opposite at "symmetry plane".

Differently from the preliminary study, in the "*Continua*" section of the CPC model, K-ω turbolence is applied. The K-ω turbulence model is widely used to simulate turbulent flow in computational fluid dynamics (CFD), particularly in simulations where near-wall behavior is significant. It offers several advantages in various applications, particularly in boundary layer flows and wall-bounded turbulence.

Nevertheless it tends to be more computationally expensive. In general, the advantages of the K-ω model make it more suitable for the current geometry.

The main remaining conditions are the same as in the preliminary study as follows:

- Steady State
- Coupled Energy
- Ideal Gas
- Coupled Flow

CPC air

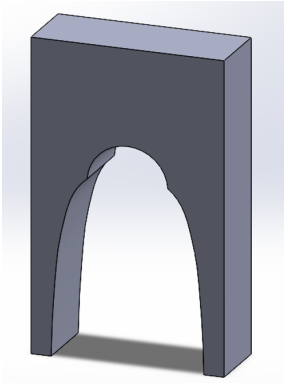

Figure 33: CPC air domain

As represented in Figure 33, the CPC frame (Compound Parabolic Collector) is typically designed as a perforated or open trapezoidal shape, which allows airflow to pass through it. This setting has specific purposes in the system's performance and efficiency. The air, working as a coolant, helps to dissipate excess heat, preventing the CPC frame from overheating and ensuring optimal operation. It is able to extend the lifespan of components and reduce thermal stresses that could lead to failure over time.

Furthermore, in systems where high temperatures can produce pressure differences within the structure, the perforation allows air to equalize the pressure between the interior and the external environment.

Indeed, the perforated trapezoidal design, besides being more economically sustainable, does not add excessive weight on the structure, and inhibits the conduction losses, that there would be if the frame were not punctured.

Air is treated as an ideal gas, and its temperature is set to 300 K.

- **Material:** Air (Ideal Gas)
- **Density:** 1.086 (kg/m^3)
- **Conductivity:** 0.026 (W/mK)
- **Specific Heat:** 1003.6 (J/kgK)

The CPC air modeling follows the same characteristics of the external air one, thus with the adoption of the K-ω turbolence model.

Instead, regarding "*Boundaries*", the entire body is set at "wall" condition.

CPC frame

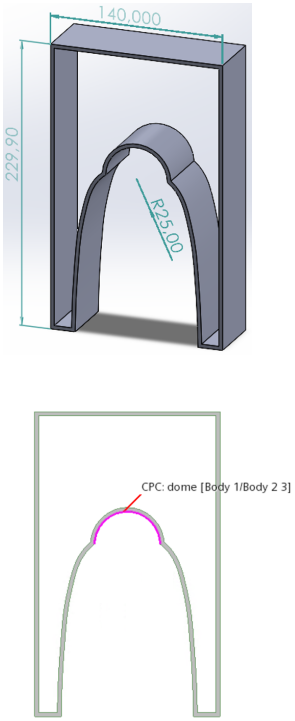

Figure 34: CPC geometry

The Compound Parabolic Concentrator (CPC), as shown in Figure 34, is 3 mm thick and owns an upper cavity within, with a radius of 25 mm. The current CPC frame does not present a flat glass plate at the bottom, to close and eventually enhance the insulation. It is open to the external environment.
The role of the dome is crucial in the project because its surface is the thermal driver of the entire model, in fact, it is set at a fixed temperature and is the promoter of the radiation emitted through the cavity.
Usually the CPC is made out of reflective aluminum because its high reflection and small absorptance coefficients make the inner part able to reconcentrate the incident sunlight radiation on the absorber tube.
Instead, in the current study, without any presence of absorbers, the internal part of the CPC, specifically the dome, is simulating the ideal positioning and functioning of a receiver, thus its properties are considered the same of a normal absorber unit.

In addiction, the CPC is made from different materials, usually the same used for making the absorber unir. It is composed by stainless steel, specifically AISI 321, a material that offers excellent resistance to elevated temperatures and is commonly used in applications where high thermal and chemical stability is required. It is also resistant to intergranular corrosion due to the presence of titanium, which prevents the formation of chromium carbides.

Talking about materials which are able to enhance the reception of the heat, coatings play a key role. There are two main categories of Solar Thermal Absorber Coatings (STACs) focused on different aspects of how they interact with solar energy and thermal energy:

- **Spectrally Selective Coatings (SSCs)**: They are able to maximize solar absorptance (α), to absorb as much solar radiation as possible and to minimize thermal emissivity (ϵ), to reduce the amount of heat emitted, thereby keeping the absorbed energy more effectively trapped.

  The goal is to have high absorption of solar energy while not losing too much heat, which is important for improving energy efficiency in solar applications.

- **High Solar Absorptance (HSA) coatings**, they focus primarily on maximizing solar absorptance α, meaning they are designed to absorb as much solar energy as possible, with less concern about how much heat is emitted.

The opto-thermal efficiency (η_{opt-th}), 19, called $\eta_{receiver}$ in the "Introduction", describes the efficiency of the coating in utilizing both the solar energy absorbed and how effectively it retains that energy (through minimizing heat loss).

The relative importance of these two factors, α (solar absorptance) and ϵ (thermal emissivity), depends on how the coating is designed to perform in specific applications.

$$\eta_{opt-th} = \frac{\alpha_{sol}\dot{q}''_{sol} - \epsilon_{th}\sigma T^4_{sol}}{\dot{q}''_{sol}} \tag{19}$$

In the current study, the inner cavity of the CPC, playing the role of the absorber, is coated with PYROMARK 2500. It is a high-performance ceramic coating, primarily designed for protecting substrates exposed to extreme heat and thermal cycling, and it guarantees high absorptance and high emissivity to the surface. Thus, PYROMARK 2500 belongs to HSA coatings; it is bigger goal is to maximize the absorptance without caring about losses.

In conclusion, the main features of the CPC frame are the following:

- **Material:** Stainless Steel (AISI 321)
- **Thickness:** 3 mm
- **Conductivity:** 20 (W/mK)
- **Density:** 8027 kg/m^3
- **Specific Heat:** 500 J/kgK
- **Coating:** PYROMARK 2500
- **Absorptance(α):** 0.95
- **Emissivity (ϵ):** 0.84

.

As said before, the dome is the thermal driver of the system, and the CPC with its characteristics is modeled for activating radiative emissions.

The "*Continua*" section differs from the fluid nature of the two previous components, and is mainly implemented as follows:

- Steady
- DOM (Discrete Ordinates Method) radiation model
- Coupled Solid Energy
- Gray thermal radiation

DOM radiation model offers high accuracy and works well in complex geometries with directional variations in radiation.

Indeed, the gray thermal radiation model is suitable for medium with constant absorption and emission properties, over all wavelengths. It is costly-effective and efficient, and can be used in high-temperature applications, where spectral variations do not play a significant role.

The radiation temperature is set at 300 K; the value at which radiation model activates itself, because the external air temperature and the air within CPC are fixed at 300 K.

Mesh scene

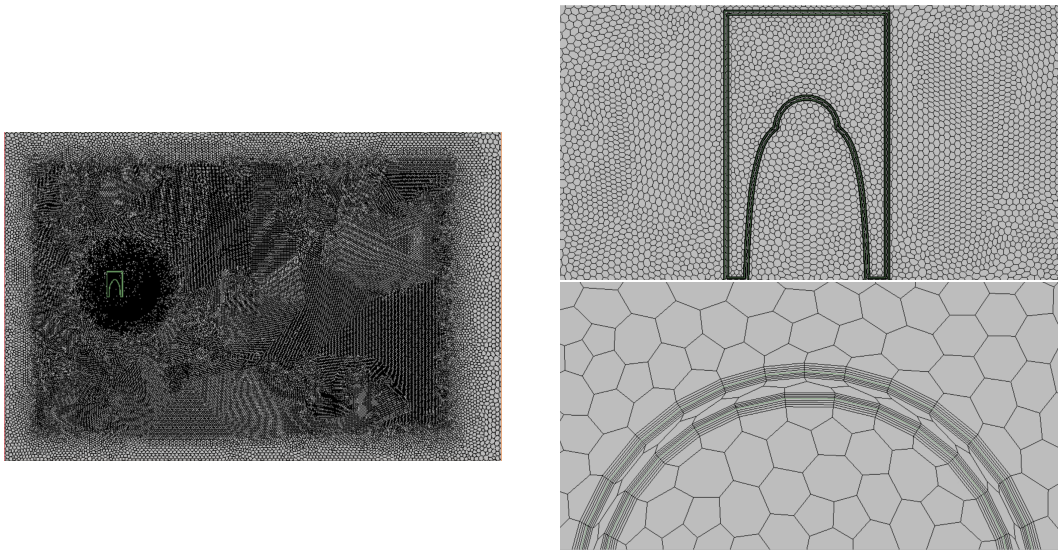

Figure 35: Meshing of CPC model

The mesh scene, shown in Figure 35, is an "Automated 2D Mesh" implemented with polygonal and prism layer mesher, and underlines the following characteristics:

- Base Size = 0.07 m
- Surface Growth Rate = 1.07
- Target Surface Size = 100%
- Minimum Surface Size = 10%
- Number of Prism Layers = 4
- Prism Layer Stretching = 1.1
- Prism Layer Thickness = 1e-3 m

Mesh	**1**	**2**	**3**	**4**	**5**	**6**	**7**	**8**
N°cells	84999	94739	116085	134290	160619	188794	235357	888934
Q (W/m)	2043	2037	2033	2021	2020	1996	1970	2054
NU	37.8	37.5	37.3	36.7	36.6	35.4	34	38.4
Ts (K)	537.3	537.5	538.4	541.4	538.4	544.7	549	542.9
Wall Y+	0.55							

Table 7: Independence mesh study CPC model 500°C - 5 m/s

As shown in 7, even if the mesh appears more dense, the results seem to be quite stable, producing slight variations in Q and Nu calculations. Increasing the number of current cells to $8.5 * 10^5$ to $8.8 * 10^6$, produces a fluctuation of Q and Nu of 0.5% and 1.5%, respectively.

Indeed, also the average temperature of the inner walls of the CPC frame undergoes a slight variation, around 1%.

Obviously, to make the mesh more dense means to rise the computational time of the model. Thus, considering computational time and accuracy of results

important at the same time, the current mesh, formed by $8.5 * 10^5$, is valuated reliable.

Indeed, the value of Wall $Y+$ is quite constant and fixed below 1, confirming the reliability of the current mesh near boundary layers.

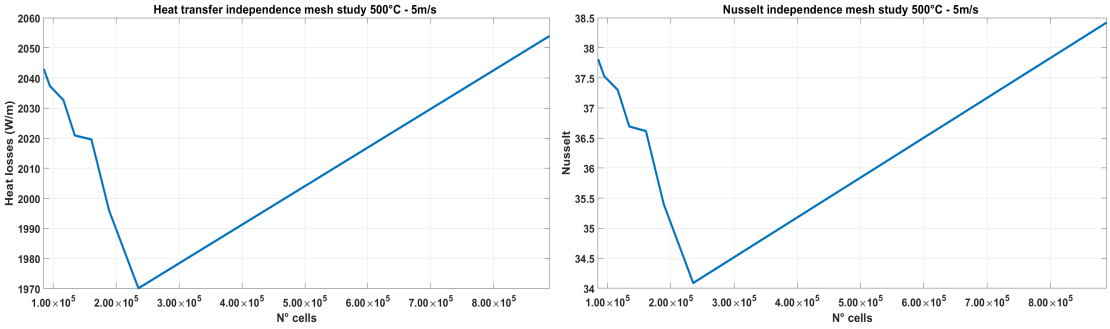

Figure 36: Q and Nu trends, independence mesh study CPC model 500°C - 5 m/s

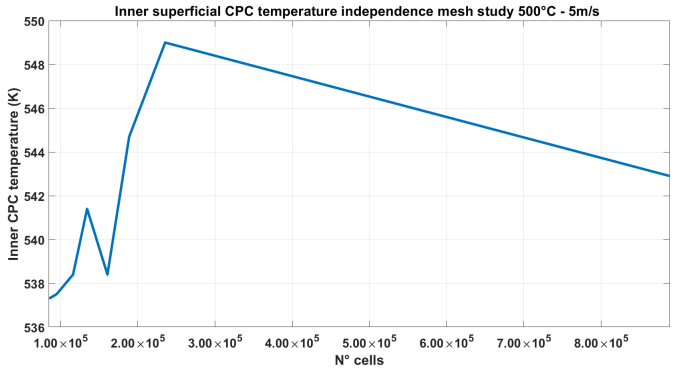

Figure 37: Average inner CPC temperature trend, independence mesh study 500 - 5 m/s

CFD analysis of the CPC model

In this chapter CFD analysis on the explained CPC model are performed.

Results are showing several radiation + convection modeling analysis, to underline the relative share and weight of both, in the total heat losses study.

In particular, the current CPC model is compared with the predefined configuration without CPC and the Shokrnia-Cagnoli design, to confirm its proper functioning and competitiveness. Starting from the study of velocity and temperature fields, arriving to Nu vs Re analysis, the current CPC frame is evaluated in several views, trying to reiterate its impact in the insulation of the area within it.

CFD calculations are computed in a wide range of velocity, 2 to 10 m/s, and temperature, 200 to 500 °C. The aim is to simulate all possible working conditions of the receiver unit and the several heat transfer fluids treated in the study.

- Molten Salt Mixture (60%wt. $NaNO_3$ + 40%wt. KNO_3): 290 – 500 °C
- Therminol VP-1: 290 – 400 °C
- DelcoTerm Solar E15: 200 – 300 °C

As explained before, the current CPC model does not present an absorber tube, replaced in his role by the CPC itself, its inner cavity. Firstly, the system has been evaluated considering only the convection model, then a convection + radiation configuration. The comparison between the two models certifies the reliability of the convection + radiation one, the only one described and useful in the current project.

Velocity field

The velocity layout explains how the CPC frame can impact the insulation of the receiver tube.

As shown in Figure 38, the wind speed, blowing from the left, is partially blocked and deviated by the external side of the "shell". The inner part of the CPC is not so much affected directly by the velocity field.

Obviously, it is fair to say that the computed analysis is simulating a totally normal wind speed field with respect to the frame, so an ideal condition. In fact in different cases, like a wind field blowing transversely, the impact would be different, highlighting the need of insulating the bottom part with a flat glass plate.

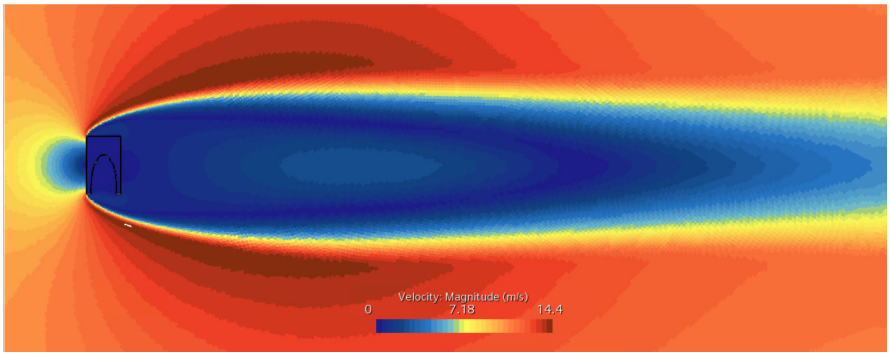

Figure 38: Velocity field CPC model 500°C - 10 m/s

it is also worth mentioning that the hypothetical positioning of the absorber tube would be towards the bottom side of the CPC, to ensure a low acceptance angle θ that allows a better sun reception from the lens. Thus, theoretically, the velocity field would have a higher impact on performances.

The vector field in Figure 39 underlines another important aspect of the study. With respect to the forced convection preliminary study, the positive interference created by the velocity field is less impacting.

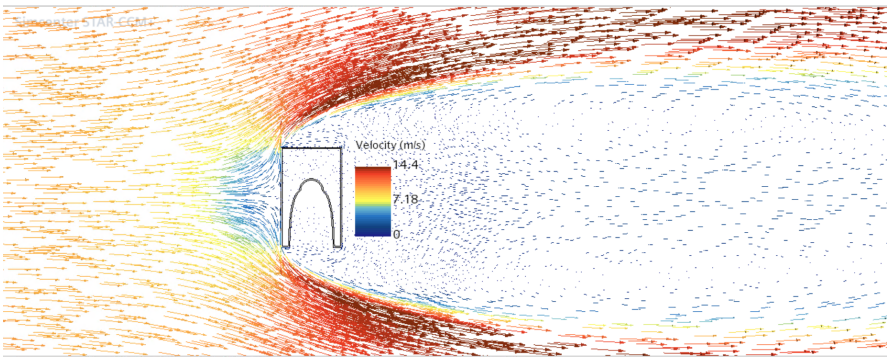

Figure 39: Vector field CPC model 500°C - 10 m/s

The CPC, thanks to its flat side structure, seems to be able to act a more important deflection of velocity vectors. In fact, the peak speed is registered at 14.4 m/s with respect to the one of forced convection model, 15.9 m/s.

Temperature field

The temperature field is an important key parameter in the current CFD analysis. As said previously, the system is evaluated in the temperature range from 200 to 500 °C, to simulate the employment of each possible working heat transfer fluid.

The Figure 40 shows the behavior of the internal part of CPC where the absorber tube should be. The thermal driver is the upper dome, set , in this case, at 500 °C, with the wind velocity shifting from 2 to 10 m/s.

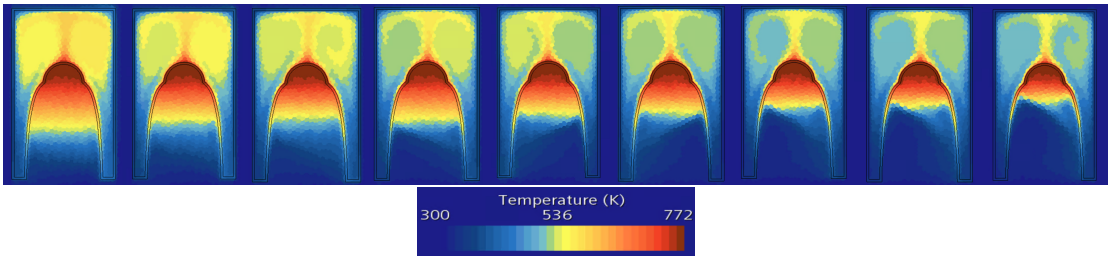

Figure 40: Temperature field CPC model (2-10 m/s - 500°C)

Obviously, from the left to the right, from 2 to 10 m/s, total heat losses registered on the surface of the CPC dome (25 mm * π) increase. The radiation share is quite constant, while the convective one rises proportionally with the wind speed.

In addiction, the temperature gradient $\frac{\partial T}{\partial y}$ is higher, increasing the velocity; each isothermal zone is smaller and spread less [20].

The inner behavior of the air flowing through the puctured trapezoidal CPC shape is an additional key parameter. The distribution of temperature is less and less spread with the rise of wind speed. Convection losses are higher and the CPC air motion is more enhanced.

This behavior underlines how the wind field, even if is not able to enter directly within the CPC, is able to affect the T field just acting on the external CPC side.

In fact the CPC frame, due to its low thickness, does not totally ensure a perfect insulation. Thin external walls, exposed to increasing forced wind convection, decrease their own average surface temperature, influencing air between the CPC frame and the dome, resulting in more heat losses of the dome itself.

CPC heat losses

Considering the radiation + convection model as the definitive final configuration, it is possible to evaluate how the CPC reacts to the simulation of different operating conditions. The entire ranges of velocity and temperature are taken into account. Figure 41 can show the path of total heat losses released by the inner cavity. Q_{tot} is the result of the sum of the convective and radiative shares [19], [22].

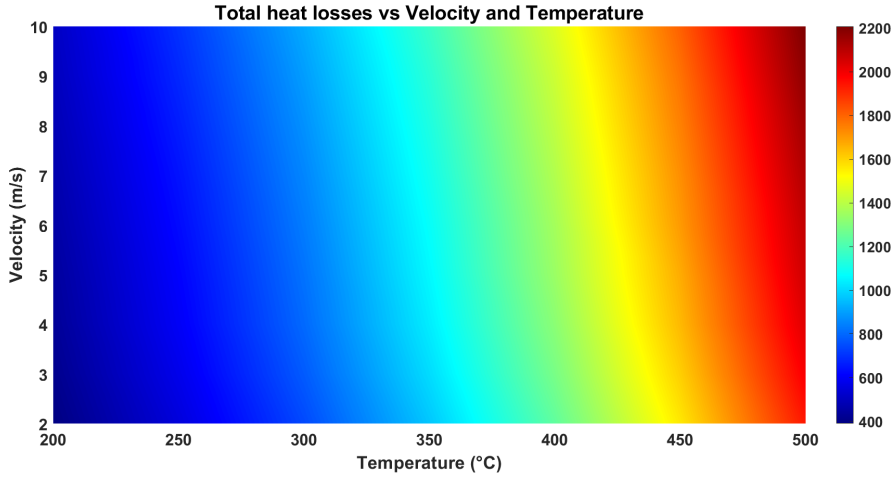

Figure 41: Total heat losses of the inner cavity vs. Temperature and Velocity

To better underline the partial weight of convection and radiation in the total heat (Q_{tot}) released by the upper cavity, the 5 m/s model is the only one reviewed. Figure 42 shows that the total heat losses in the temperature range follow an exponential trend. Specifically, the radiative share is the one responsible for shaping the dome losses like that, following Stefan-Boltzmann equation.

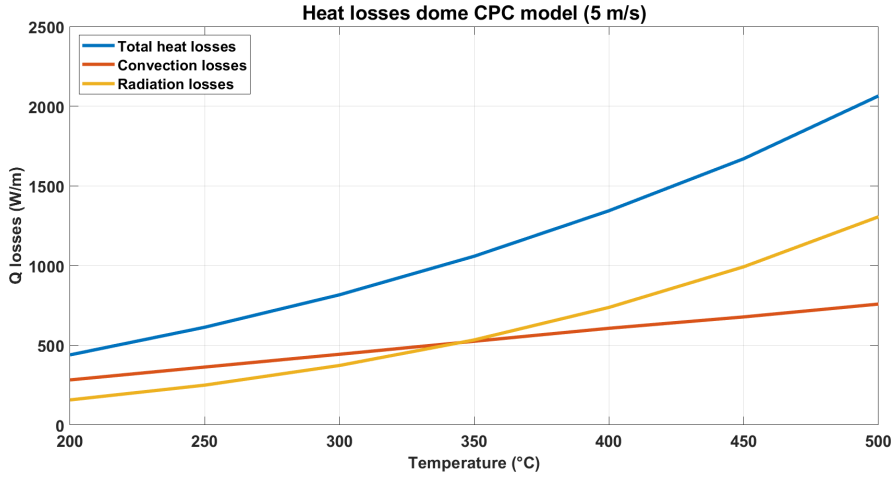

Figure 42: Total dome heat losses with convective and radiative share CPC model 5 m/s

Stefan-Boltzmann law states that the total energy radiated by a perfect black body (an object that absorbs all incoming radiation) is directly proportional to the fourth power of its absolute temperature (K). This means that as the temperature

of a body increases, the amount of energy it radiates grows much faster, following a T^4 dependency, as represented in Eq.20.

$$Q_{\text{rad}} = A_{\text{dome}} \cdot \sigma \cdot \epsilon \cdot \left(T_{\text{dome}}^4 - T_{\text{amb}}^4\right) \tag{20}$$

Where:

- Q_{rad}: radiative heat transfer (W)
- A_{dome}: area of the dome (m^2)
- σ: Stefan-Boltzmann constant (5.67e-8 W/m^2K^4)
- ϵ: emissivity of the material
- T_{dome}: temperature of the dome (K)
- T_{amb}: ambient temperature (K)

The current system is a simplified 2D domain, so the axial depth is considered equal to one and A_{dome} equal to 0.025 * π.

ϵ is the PYROMARK 2500 emissivity, equal to 0.84.

It is possible to notice how the total heat is distributed. With lower temperatures, the latter is more affected by the convective heat transfer, which follows the linear behavior described in Eq.10 [17], [18].

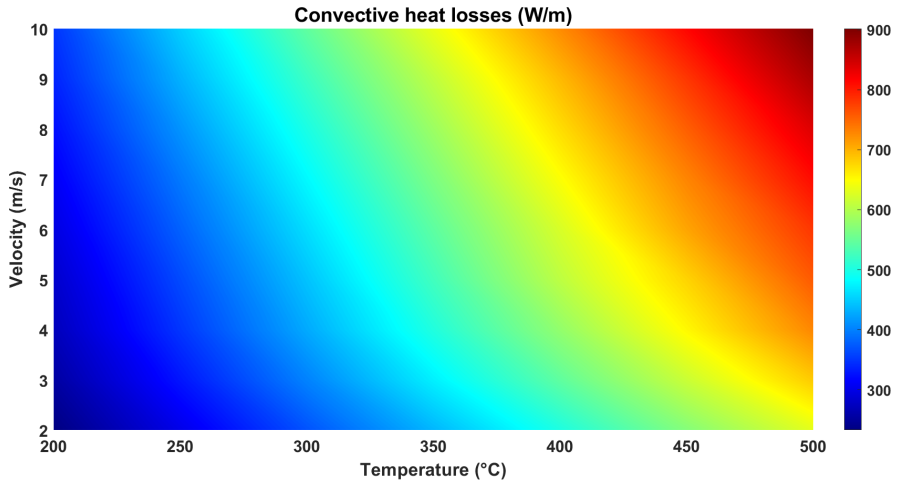

Figure 43: Convection heat losses vs. Temperature and Velocity CPC model

However, with higher temperatures, the radiation exerts a stronger influence.

The radiative share, without being affected by the wind speed, is almost fixed for the entire range of velocity.

In reality, Stefan-Boltzmann describes an ideal scenario, on the assumption that the object in question is a perfect black body and the temperature is uniform throughout its surface.

In fact, in the CFD analysis, the radiation coefficient, theoretically equal to $\sigma * \epsilon$, is not totally constant but is slightly influenced by the buoyancy motion of the fluid in the internal part of the CPC, resulting in a surface temperature not totally uniform.

However, is being talking about small and almost negligible variations. Considering the radiation coefficient constant, results are the following:

Temperature (°C)	200	250	300	350	400	450	500
Q_{rad} (W/m)	157.1	249.8	373.2	533.5	737.44	992.25	1305.7

Table 8: Radiative heat transfer of CPC model 200 - 500 °C

On the other hand, the presence of wind speed has a much stronger impact on the share of convective heat losses, as already represented in 43.

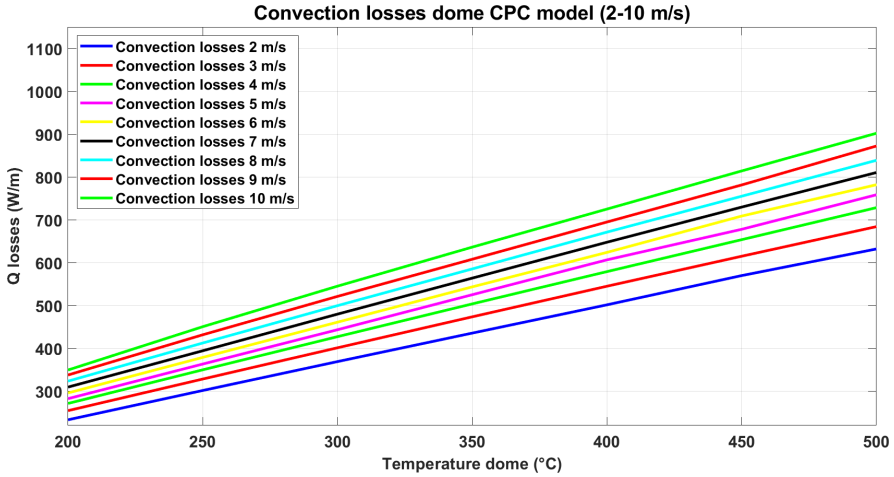

Figure 44: Convection losses vs. Velocity CPC model

Analyzing Figure 44, it is right to point out that the variation of the wind speed from 2 m/s to 10 m/s causes an overall increase of the convective losses equal to 50%.

Making a comparison with the preliminary study, it is possible to visualize the massive effect made by the CPC on the convective transfer.

Even if in the forced convection preliminary study the temperature is much lower, the convective heat losses result to be much higher. It is fair to say that the considered areas are different; however, the overall gap remain quite important.

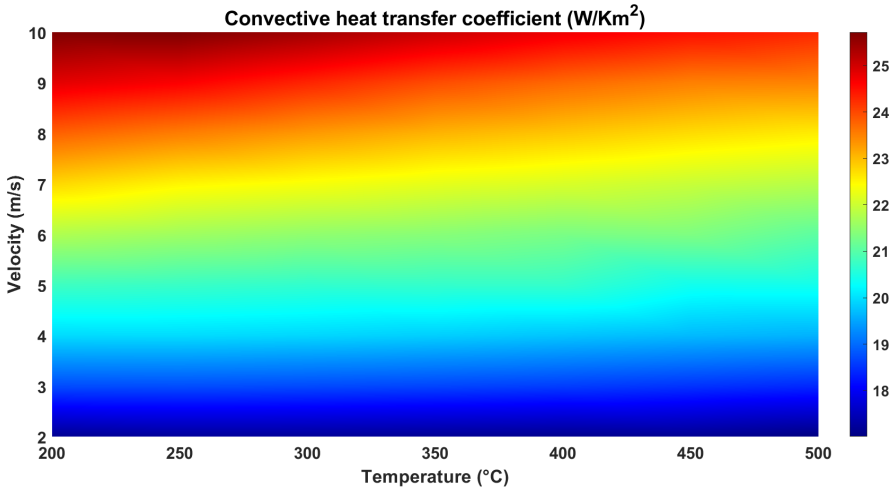

Figure 45: HTC evolution vs. Temperature and Velocity CPC model

Regarding the convective heat transfer coefficient h, as represented in Figure 45, it gains value proportionally to the increment of the wind speed, while it is almost constant considering an increasing temperature.

The increase of wind speed from the left side of the domain causes an enhancement of the buoyancy motions in the position of the absorber tube and in the air between the CPC frame. In fact, also the average surface temperature of the internal side reflects this behavior. As represented in Figure 46, as the velocity rises, the average $Tsurface$ linearly decreases.

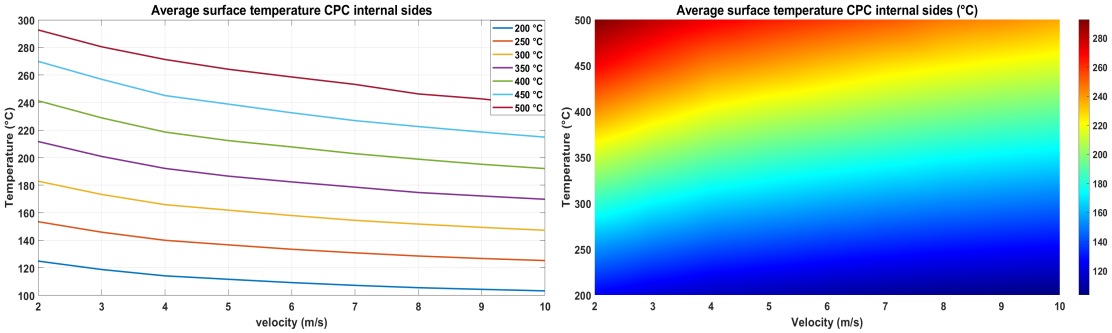

Figure 46: Average surface temperature of CPC internal sides

CPC comparison study

This section points out a comparative evaluation made on the applied CPC frame, in the current domain. Figure 47 underlines the improvements in heat transfer after the implementation of the CPC.

The slope of the trend lines, which simulate the current project (green), indicates how, with the presence of the CPC frame, the system is able to manage the maximum temperature (ideal condition) without reporting so much more heat losses.

Considering Zhukauskas as the reference model, a massive drop is being produced. While maintaining fixed temperature and making the velocity varying, and viceversa, around 50% of the heat losses derived from convection motion, integrated into the analysis limits, are cut, reporting a particularly enhanced response with stronger temperature and velocity fields.

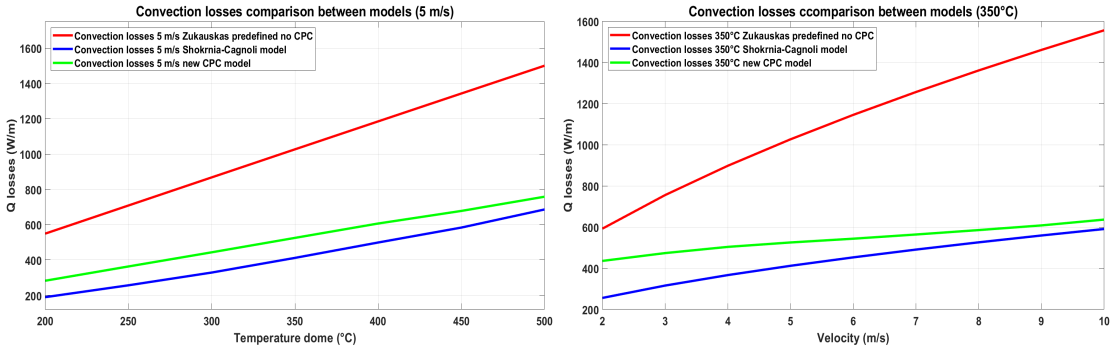

Figure 47: Comparisons between CPC models about convection losses vs. temperature and velocity fields

In fact, as the Q vs. v graph shows, the increase in wind speed from the left of the domain does not cause a so relevant growth in convection transfer, as expected, and as shown by Zhukausas. This trend seems to be almost uniform throughout the field.

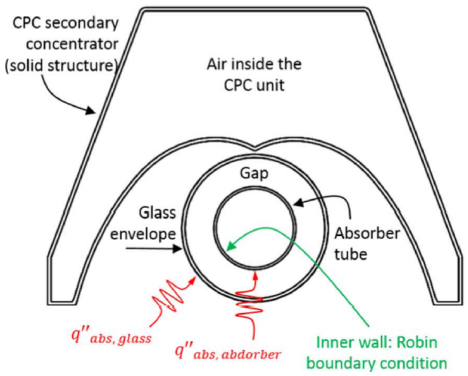

Instead, the blue line represents the following Eq.21, recovered in [17], that describes the behavior of the Shkornia - Cagnoli model, where the absorber tube is protected by another CPC frame, with different geometry and performances.

Figure 48: Shkornia - Cagnoli receiver unit geometry

$$Nu = 0.165 \cdot \left(\mathrm{Re}^{0.52}\right) \cdot \left(\mathrm{Pr}_{\mathrm{atm}}^{0.37}\right) \cdot \left(\frac{\mathrm{Pr}_{\mathrm{atm}}}{\mathrm{Pr}_{\mathrm{dome}}}\right)^{0.25} \tag{21}$$

The equation describes the convective heat motion behavior, thus, it is possible to make a comparison on convection losses, as shown in Figure 47.

It is clear that even if trends are similar, the current analyzed CPC model is not efficient as the Shkornia - Cagnoli's one [17], [18].

In addiction, it is fair to say that the considered driver of the heat transfer (inner dome) has got the ideal positioning for not being so much influenced by the parallel velocity field. In reality, the absorber tube would be set in a lower position, with a consequent worsening of the heat losses amount derived by the presence of the wind speed.

In the Shorknia - Cagnoli study the CPC geometry design, as represented in Figure 48, is different. The acceptance angle θ is lower, allowing the absorber unit to receive reflected solar light beams from a wider lens field.

Furthermore, the use of reflective aluminum on the inner part is able to reconcentrate in the best way the beams that do not directly reach the absorber tube.

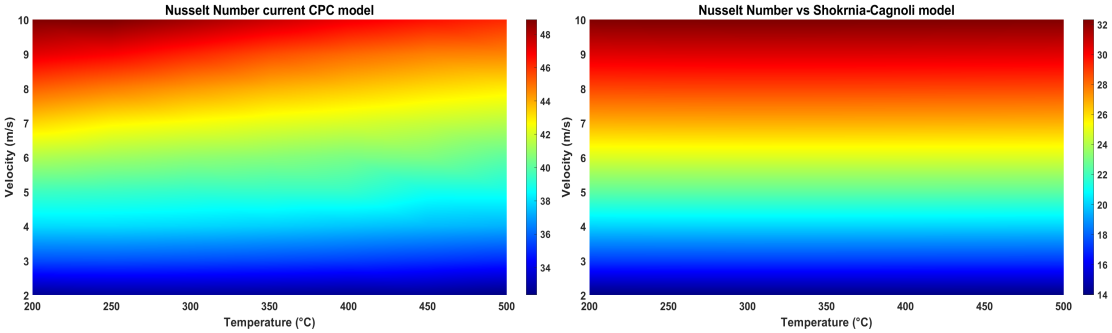

Figure 49: Nusselt comparison between Shokrnia - Cagnoli's and the current CPC model

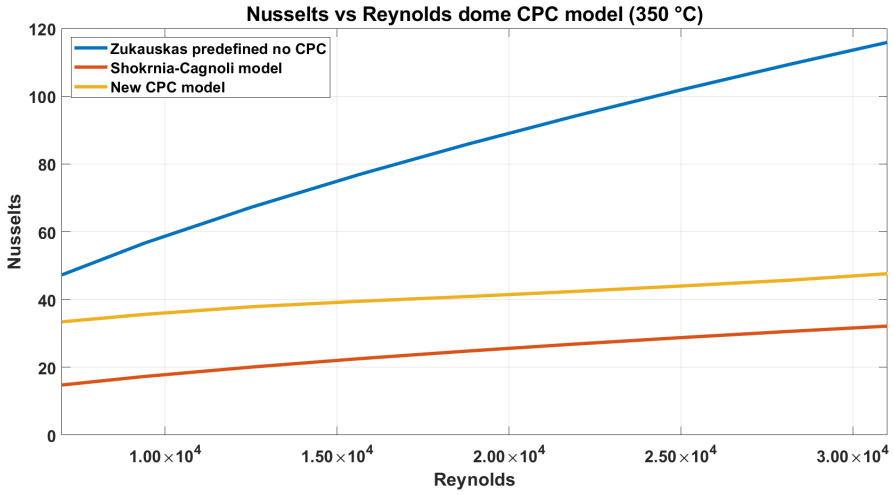

Figure 50: Nusselt vs. Reynolds comparison between CPC models

Figures 50 and 49 show evaluations of Nu, so the overall performance gap

between the current CPC design and the Shkornia - Cagnoli model with respect to velocity and temperature gradients.

The main reason to explain the performance gap in the insulation of the main unit with respect to the model analyzed in this project, is the presence of the glass envelope around the receiver. Thus, heat losses of the absorber tube are strongly affected by the presence of the latter and by the way it is installed, simply encapsulated or with vacuum between the glass and the tube. The glass envelope gives to the receiver unit a better insulation, decreasing the convective motion around the tube and providing an additional barrier against the wind.

This condition gives to the current study margins, because the current CFD domain does not foresee that insulation configuration.

In fact, if the same condition was implemented, the heat transfer behavior would improve, the convection heat losses would undergo a sharp drop and the retention of temperature would be more effective. Thus the current CPC geometry could still be competitive with respect to previous models and could be a concrete option than other geometry configurations.

Obviously further calculations and evaluations have to be done for better assessing the real value of the examined system and make it suitable for real application.

Nusselt correlation

To provide a reference to the examined CPC design, after a detailed evaluation of its performance, it is possible to provide the following correlation:

$$\mathrm{Nu} = 4.66 \cdot \mathrm{Re}_D^{0.233} \cdot \mathrm{Pr}_{atm}^{0.37} \cdot \left(\frac{\mathrm{Pr}_{atm}}{\mathrm{Pr}_{dome}} \right)^{\frac{1}{4}} \tag{22}$$

The Eq. 22 has the same design of Zhukauskas correlation.

Where 4.66 and 0.233 are the coefficients obtained through the employment of an optimization model. The latter is able to read all registered data provided by CFD models and to give outputs which are able to provide the correct simulation of the system behavior.

Parameters Re_D and Pr_{atm} are evaluated at ambient temperature. The absorber tube is replaced by the upper cavity of the CPC frame, thus the ratio $\frac{\mathrm{Pr}_{atm}}{\mathrm{Pr}_{dome}}$ underlines the behavior of the dome in the system.

The obtained correlation is able to provide a detailed prediction of the current CPC model, specifically its convective motion behavior, as shown in Figure 51.

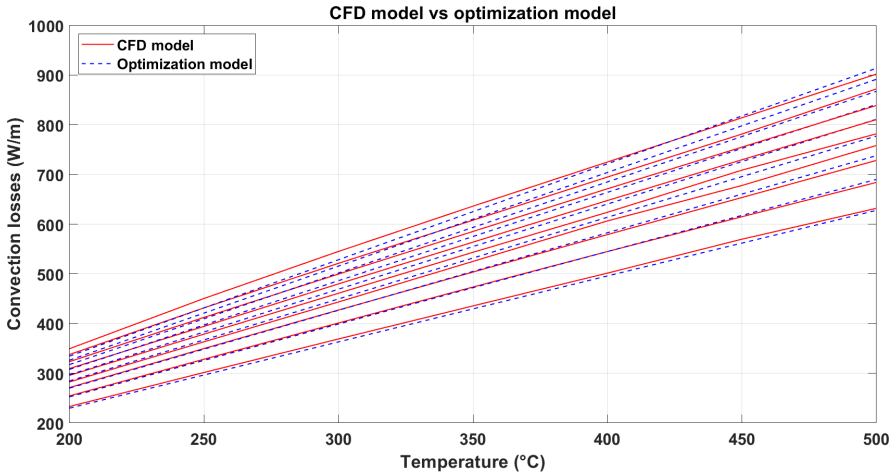

Figure 51: Optimization model prediction for new Nu correlation

Optimization model

The algorithm used is quasi-Newton, an iterative optimization method aimed at minimizing an objective function.

The quasi-Newton method is a family of numerical methods that aim to find the minimum of a function (in this case, the objective function defined as the sum of squared differences between the model and observed data).

The main advantage of quasi-Newton methods over classic Newton methods is that they do not require the explicit calculation of the Hessian matrix (which contains the second derivatives of the objective function), but instead, they approximate it iteratively.

The current objective function calculates the squared difference between the model (with the current parameters) and the observed data. Then, the optimization step aims to minimize this difference, thus to find the zero.

The total algorithm is shown in A.

The $fminunc$ is a MATLAB optimization function, that in this case, tries to find the optimized values of B (4.66) and a (0.233) which are enabled to minimize the objective function.

Conclusion

In conclusion, the current CPC geometry could still remain competitive when compared to previous models and might even present a more viable option than other geometric configurations.

However, it is important to recognize that further detailed calculations and evaluations are necessary in order to more accurately determine the true performance of the system.

Only after conducting these assessments it is possible to properly judge its potential and make adjustments to ensure that it is suitable for real-world applications. These further studies will help refine the design and evaluate how effectively the system can be implemented on a practical scale.

In addiction, an economical evaluation would provide a different sight on the current design, giving to the work another benchmark with respect to other geometries. The application of different materials, coatings, heat transfer fluids and obviously different outputs are variables to be considered in the economical assessment.

The vision of the current project is to make room to the LFC technology, to make it comparable with the more widespread PTC configuration.

Concentrated solar power (CSP) systems are currently an underutilized energy source within the broader field of renewable energy. Despite the potential they hold, these systems have not yet been fully developed or widely adopted. There is still significant untapped potential for CSP to contribute to the generation of clean, sustainable energy. However, the lack of widespread implementation means that CSP is not yet playing as large a role in the renewable energy landscape as it could.

A diversified renewable energy portfolio mitigates the risks associated with over-reliance on a single source of energy. By leveraging the strengths of different Renewable Energy Sources (RES), countries can smooth out fluctuations in energy production and better balance supply with demand.

The integration of multiple RES also offers a strategic advantage from an energy security perspective. With a diverse energy mix, countries can reduce their dependence on external energy imports and increase their energy independence. This is especially critical in the context of geopolitical tensions and energy supply disruptions, where a diversified portfolio ensures that nations are less vulnerable to market fluctuations and energy crises.

Thus, each RES plays a crucial role in the energy sector transition, because its effects propagate along all country assets. CSP must to be considered as impactful as the other RES.

Appendix A

Optimization function

```
%%
vel=[2 3 4 5 6 7 8 9 10]';
dens=1.165;
visc=186e-7;
re=dens*vel*0.050/visc;
pr_atm=0.7282;
pr_dome=[0.6974 0.6946 0.6935 0.6937 0.6948 0.6965 0.6986];
kk=0.0263;

h_conv_cfd=[17.26 17.3 17.28 17.22 17.17 17.19 17.05;
    18.85 18.83 18.79 18.73 18.65 18.56 18.46;
    20.09 20.07 20.08 19.92 19.83 19.73 19.65;
    20.92 20.84 20.76 20.77 20.76 20.46 20.46;
    21.91 21.73 21.59 21.5 21.36 21.39 21.1;
    22.92 22.62 22.47 22.3 22.17 22.02 21.87;
    23.94 23.66 23.39 23.15 22.98 22.79 22.63;
    25 24.76 24.41 24.05 23.79 23.58 23.53;
    25.87 25.85 25.53 25.16 24.82 24.57 24.34];

Nu_conv=h_conv_cfd.*0.05/kk;

[Re_expanded, Pr_dome_expanded] = ndgrid(re, pr_dome);

% Calculation of matrix C based on Pr
C_expanded = (pr_atm^0.37) * ((pr_atm ./ Pr_dome_expanded) .^ 0.25);

% Conversion matrix in vector
Zhukauskas_flat = Nu_conv(:);

% Model creation
model = @(params, re, C) params(1) * (re .^ params(2)) .* C;

% Objective function (sum of squared differences between the model
    and observed data)
objective = @(params) sum((model(params, Re_expanded(:), C_expanded
    (:)) - Zhukauskas_flat).^2);

%Initial parameters
```

```
37 params_initial = [0.5, 0.5];
38
39 % Optimization function: fminunc
40 options = optimoptions('fminunc', 'Display', 'iter', 'Algorithm', '
       quasi-newton', ...
41                        'TolFun', 1e-6, 'TolX', 1e-6, 'MaxIter', 1000)
       ;
42
43 [param_optimized, fval] = fminunc(objective, params_initial, options)
       ;
44
45 % Results
46 B_optimized = param_optimized(1);
47 a_optimized = param_optimized(2);
48
49 disp(['Valore ottimizzato di B: ', num2str(B_optimized)]);
50 disp(['Valore ottimizzato di a: ', num2str(a_optimized)]);
```

Bibliography

[1] ClimateWatch. *Historical GHG Emissions*. 2021. URL: https://www.climatewatchdata.org/ghg-emissions?chartType=area&end_year=2021&sectors=energy&start_year=1990 (cit. on p. 2).

[2] Francesco Laio. «Cambiamenti climatici e socio economici». In: *Global greenhouse gas emission by sector*. 2022 (cit. on p. 3).

[3] Copernicus. *Annual global surface temperature*. 2024. URL: https://climate.copernicus.eu/why-do-we-keep-talking-about-15degc-and-2degc-above-pre-industrial-era (cit. on p. 3).

[4] Parlamento italiano. *L'attuazione del Protocollo di Kyoto*. 2012. URL: https://leg16.camera.it/561?appro=9 (cit. on p. 5).

[5] Sandra Day O'Connor Danel Bodansky. *Historical GHG Emissions*. 2021. URL: https://www.climatewatchdata.org/ndc-overview (cit. on p. 5).

[6] ClimateWatch. *Paris Agreement*. 2023. URL: https://legal.un.org/avl/ha/pa/pa.html (cit. on p. 5).

[7] Richard Perez Marc Perez. «A fundamental look at supply side energy reserves for the planet». In: *ELSEVIER* (2022). URL: https://www.sciencedirect.com/science/article/pii/S266711312200002X?via%3Dihub (cit. on p. 7).

[8] Michael Taylor Roland Roesch. «Renewable power generation costs in 2022». In: *IRENA* (2023). URL: https://www.irena.org/-/media/Files/IRENA/Agency/Publication/2023/Aug/IRENA_Renewable_power_generation_costs_in_2022.pdf (cit. on pp. 7, 8).

[9] Global Solar Atlas. *Horizontal solar irradiation capacity*. 2025. URL: https://globalsolaratlas.info/map (cit. on p. 9).

[10] IRENA. *Solar energy*. 2024. URL: https://www.irena.org/Energy-Transition/Technology/Solar-energy (cit. on p. 9).

[11] Simon Caron Heller. «Opto-thermal analysis of solar thermal absorber coatings under concentrated solar radiation based on spectral measurement techniques». In: *Escuela de Doctorado de la Universidad de Almería* (2024) (cit. on p. 10).

[12] R. Zanino M. Cagnoli. «An Introduction to Concentrated Solar Power (CSP) Technology». In: *Concentrated Solar Power (CSP) Technology*. 2023 (cit. on p. 11).

[13] REN21. *Concentrated Solar Thermal Power (CSP)*. 2023. URL: https://www.ren21.net/gsr-2024/modules/energy_supply/02_market_and_industry_trends/02_csp/#:~:text=The%20world's%20largest%20CSP%20plant,of%20the%20end%20of%202023. (cit. on p. 11).

[14] Wikipedia. *Concentrated solar power*. 2025. URL: https://en.wikipedia.org/wiki/Concentrated_solar_power (cit. on pp. 12, 14, 15).

[15] Matthias Günther. «Linear Fresnel Technology». In: *Advanced CSP Teaching Materials*. 2023 (cit. on p. 12).

[16] Manuel Collares-Pereira Diogo Canavarro Julio Chaves. «Simultaneous Multiple Surface method for Linear Fresnel concentrators with tubular receiver». In: *ELSEVIER* (2014) (cit. on p. 14).

[17] Roberto Zanino Mehdi Shokrnia Mattia Cagnoli. «Comparative optical, thermal and economic analysis of parabolic trough and linear Fresnel collectors with evacuated and non-evacuated receiver tubes». In: *Dipartimento Energia, Politecnico di Torino* (2024) (cit. on pp. 14, 43, 46, 47).

[18] Zanino Cagnoli. «Analysis of the performance of linear Fresnel collectors: Encapsulated vs evacuated tubes». In: *ELSEVIER* (2018) (cit. on pp. 14, 31, 43, 47).

[19] T. Sundararajan K.S. Reddy Shanmugapriya Balaji. «Estimation of heat losses due to wind effects from linear parabolic secondary reflector ereceiver of solar LFR module». In: *ELSEVIER* (2018) (cit. on pp. 21, 26, 42).

[20] Mojtaba Mamourian Kamel Milani Shirvan. «Numerical study of surface radiation and combined natural convection heat transfer in a solar cavity receiver». In: *International Journal of Numerical Methods for Heat Fluid Flow* (2017) (cit. on pp. 21, 27, 41).

[21] Frank P. Incropera, David P. De Witt, Theodore L. Bergman, and Adrienne S. Lavine. *Fundamentals of Heat and Mass Transfer*. John Wiley Sons, 2007 (cit. on pp. 22, 23, 28, 29).

[22] Vishwa Mohan Behera Satish Ranjan Pradhan. «Study of combined effect of natural convection and radiation heat transfer from annular finned vertical cylinder». In: *National Institute of Technology Rourkela, India* (2022) (cit. on p. 42).

Acknowledgements